# On the use of frequency-swept pulses and pulses designed with optimal control theory for the acquisition of ultra-wideline NMR spectra

Adam R. Altenhof [a], Austin W. Lindquist [b], Lucas D.D. Foster [b], Sean T. Holmes [a], Robert W. Schurko [a,*]

[a] Department of Chemistry and Biochemistry, Florida State University, Tallahassee, FL 32308, United States
[b] Department of Chemistry and Biochemistry, University of Windsor, Windsor, ON N9B 3P4, Canada

ABSTRACT

Frequency-swept (FS) pulses, such as wideband uniform-rate smooth-truncation (WURST) pulses, have found much success for the acquisition of ultra-wideline (UW) solid-state NMR spectra. In this preliminary study, new pulses and pulse sequences are explored in simulation and experimentally for several nuclei exhibiting UWNMR powder patterns under static conditions, including $^{119}$Sn ($I = 1/2$), $^{195}$Pt ($I = 1/2$), $^{2}$H ($I = 1$), and $^{71}$Ga ($I = 3/2$). First, hyperbolic secant (HS) and tanh/tan (THT) pulses are tested and implemented as excitation and refocusing pulses in spin-echo and Carr-Purcell/Meiboom Gill (CPMG)-type sequences, and shown to have comparable performances to analogous WURST pulses. Second, optimal control theory (OCT) is utilized for the design of new Optimal Control Theory Optimized Broadband Excitation and Refocusing (OCTOBER) pulses, using carefully parameterized WURST, THT, and HS pulses as starting points. Some of the new OCTOBER pulses used in spin-echo sequences are capable of efficient broadband excitation and refocusing, in some cases resulting in spectra with increased signal enhancements over those obtained in experiments using conventional FS pulses. Finally, careful consideration of the spin dynamics of several systems, by monitoring of the time evolution of the density matrix *via* the Liouville-von Neumann equation and analysis of the time-resolved Fourier transforms of the pulses, lends insight into the underlying mechanisms of the FS and OCTOBER pulses. This is crucial for understanding their performance in terms of generating uniformly excited patterns of high signal intensity, and for identifying trends that may offer pathways to generalized parameterization and/or new pulse shapes.

© 2019 Elsevier Inc. All rights reserved.

## 1. Introduction

Many solid-state NMR (SSNMR) spectra are difficult to acquire due to severely inhomogeneously broadened patterns that result from anisotropic NMR interactions, including the quadrupolar, chemical shift, and paramagnetic interactions. Spectra featuring powder patterns with breadths ranging from 250 kHz to tens of MHz are classified as ultra-wideline (UW) NMR spectra, since most often, these patterns cannot be excited uniformly with conventional rectangular pulses – such UWNMR spectra are often acquired with pulse sequences featuring shaped pulses, specialized hardware, and/or high magnetic field strengths [1]. Acquisition of UWNMR spectra can be complicated further if the NMR-active nuclei are unreceptive; this can be the result of a low gyromagnetic ratio ($\gamma$), low natural abundance (n.a.) and/or dilution of the nucleus of interest, unfavorable relaxation characteristics (*i.e.*, long

$T_1$ and/or short $T_2$ time constants), and any combination of these factors. As such, the design of experimental techniques that lead to improved spectral acquisitions and reductions in experimental times is of fundamental importance to NMR spectroscopists, as well as for numerous applications for the study of nuclei of elements across of the periodic table.

Historically, UWNMR patterns have been acquired using a variety of methods. Early experiments used swept magnetic fields with a fixed transmitter frequency [1,2]. However, this was largely supplanted by the use of a constant magnetic field, and stepping the transmitter across the pattern in even frequency increments (*i.e.*, the echo intensities were plotted as a function of the transmitter frequency). The latter methodology was substantially improved by the variable-offset cumulative spectroscopy (VOCS) method, in which a series of full-echo spectra are acquired at even transmitter offsets, Fourier transformed to yield individual sub-spectra, and the resulting sub-spectra co-added or projected to produce the overall pattern [3,4]. The VOCS method reduces the overall number of experiments required to generate a uniformly excited UWNMR

pattern, while providing higher spectral resolution that is not dependent on the individual transmitter offsets.

The acquisition of both wideline and UWNMR patterns has benefitted from the implementation of the Carr/Purcell–Meiboom/Gill (CPMG) sequence [5]. Used initially by Slichter *et al.* for spin-1/2 nuclei [6], and reintroduced by Larsen and co-workers for quadrupolar nuclei [7–9], this pulse sequence features repeated acquisition of refocused spin polarization, allowing for signal enhancement that is dependent upon the effective transverse relaxation time constant, $T_2^{\mathrm{eff}}$ [10]. All of the methods mentioned above feature the use of rectangular pulses, which have excitation bandwidths limited by pulse width and RF amplitude.

More recently, acquisition of UWNMR spectra has been improved by developments in hardware and pulse-sequence design. Hardware innovations include access to ultrahigh-field superconducting magnets, improvements in the design of NMR probes, and the use of microcoils, low-gamma tuning boxes, and robotic tuning [11,12]. Innovations in pulse sequence design include indirect detection methods that employ magic-angle spinning (MAS) [13–15], dynamic nuclear polarization (DNP, also hardware design) [16–19], and the use of frequency-swept pulses for a variety of direct-detection experiments; our research group has been heavily involved in this latter area [1,19].

Frequency-swept (FS) pulses can be used for broadband excitation and refocusing of spin polarization in NMR experiments. A FS pulse is one in which the amplitude and/or phase is modulated to provide a linear or non-linear virtual frequency sweep, while irradiating at a single transmitter frequency [20]. The wideband uniform-rate smooth-truncation (WURST) pulse [21] has been used extensively in UWNMR experiments [1,2]. WURST pulses were implemented in the spin-echo-style pulse sequence (WURST-echo) of Bhattacharyya and Frydman [22], and later in the CPMG-style pulse sequence (WURST-CPMG) of O'Dell and Schurko [23]. In addition, WURST pulses have been implemented for the purposes of broadband cross polarization (CP) experiments, such as the broadband adiabatic inversion-CP (BRAIN-CP) sequence [24]. All of these sequences allow for the acquisition of UWNMR spectra of a variety of unreceptive spin-1/2 and quadrupolar nuclei [2,25,26]; however, WURST pulses are still limited in terms of frequency bandwidths and the acquisition of distortionless powder patterns – sometimes by the probe characteristics (excitation and detection bandwidths) or by the pulses themselves [1]. It is possible that other classes of FS pulses can be implemented in a manner analogous to WURST pulses in the WURST-echo and WURST-CPMG experiments. Tanh/tan (THT) and hyperbolic secant (HS) pulses are types of FS pulses that have been used in a variety of magnetic resonance experiments [20,27]. THT pulses have been used in magnetic resonance imaging (MRI) [28] and for fast broadband adiabatic inversion [29]. HS pulses were introduced as analytical solutions to the Bloch equations in the Ricatti form [30]; since their introduction, HS pulses have found a wide array of applications in both NMR and MRI, for robust adiabatic inversion, satellite transition inversion for half-integer quadrupolar nuclei, and MQMAS excitation and conversion pulses [31–34]. To date, neither THT or HS pulses have been implemented in UWNMR experiments, either as direct excitation and refocusing pulses, or for continuous refocusing in a CPMG-type sequence.

It is also possible to design new pulses for the acquisition of UWNMR patterns using optimal control theory (OCT). Many pulses and pulse sequences have been designed using a variety of OCT algorithms [35–38]. For instance, Glaser and co-workers have utilized OCT to design pulses and sequences for broadband excitation (BEBOP and BIBOP) [39–42], calibration-free broadband excitation [43], linear phase dispersion and coherence transfer (ICEBERG) [44], broadband universal rotation for refocusing (BURBOP)

[45,46], applications to broadband Ramsey pulse sequences [47], relaxation dispersion (ORECA) [48], and broadband spin echoes [49]. Borneman et al. investigated the use of OCT for designing refocusing pulses in CPMG-type sequences [50]. Tosner *et al.* implemented the GRAPE algorithm of OCT into the open-source software SIMPSON [51] (in the current work, this is the software utilized for pulse design with OCT). GRAPE and other OCT algorithms have been implemented in other software, such as SPINACH [52]. To date, there are a limited number of examples of the implementation of pulses designed with OCT for the acquisition of *experimental* SSNMR powder patterns [53–55], and to the best of our knowledge, there is no work on the acquisition of UWNMR patterns using pulses developed with OCT.

Herein, three facets of pulse sequence design for the acquisition of UWNMR spectra of stationary samples (*i.e.*, no MAS) are explored: (i) the implementation of a variety of FS pulses in spin-echo and CPMG-type-sequences, including WURST, THT, and HS pulses, (ii) the use of OCT for the design of new Optimal Control Theory-Optimized Broadband Excitation and Refocusing (OCTO-BER) pulses, which utilize the aforementioned FS pulses as starting functions, and (iii) the careful examination of spin dynamics induced by different pulses and pulse sequences, in order to gain insight into their underlying mechanisms. In this preliminary study, numerical simulations and experimental implementations of these pulses and sequences are presented for several different nuclei, including $^{119}$Sn ($I = 1/2$), $^{195}$Pt ($I = 1/2$), $^2$H ($I = 1$), and $^{71}$Ga ($I = 3/2$). Finally, the potential for finding pathways to solutions for pulses at global maxima in terms of both signal enhancement and uniform excitation is discussed.

## 2. Experimental methods

### 2.1. Samples

Tin(II) oxide [SnO, Sigma Aldrich], tetraamine platinum(II) chloride monohydrate [Pt(NH$_3$)$_4$Cl$_2$·H$_2$O, Sigma Aldrich], deuterated α-glycine [α -glycine-$d_2$, Cambridge Isotope Laboratories, Inc.], and gallium(III) phthalocyanine chloride [GaPcCl, Sigma Aldrich] were purchased and used in all subsequent NMR experiments without further purification. The identities and purities of the samples were verified through comparisons with previously reported NMR spectra and PXRD patterns [23,24,55]. All samples were ground into fine powders and packed into 5 mm outer-diameter glass tubes and sealed with Teflon tape.

### 2.2. FS pulse parameters

The waveforms of the FS pulses are specified by a set of parameters that describe the RF amplitudes and phase modulations during the pulses (see the *Discussion of Frequency-Swept Pulse Functions* section in the Electronic Supporting Information, ESI). HS pulses utilized values of μ = 6.0 and β = 3.0 for $^{119}$Sn and $^2$H experiments, and μ = 8.0 and β = 5.0 for $^{195}$Pt and $^{71}$Ga experiments. THT pulses utilized values of κ = tan$^{-1}$(1.0) and ζ = 10.0 for all systems and featured sweep widths of 500 kHz for $^{119}$Sn and $^2$H, 800 kHz for $^{71}$Ga, and 1.2 MHz for $^{195}$Pt [20]. WURST pulses utilized a truncation factor of $N = 20$ and a total sweep width of 500 kHz for $^{119}$Sn and $^2$H, 800 kHz for $^{71}$Ga, and 1.2 MHz for $^{195}$Pt [25]. All FS pulses were tested with $\tau_p$ = 25 μs, 33 μs, and 40 μs, with $N_p$ = 375, 495, and 600 points, respectively, thereby fixing the dwell time of the pulse at $\tau_{\mathrm{dwp}}$ = 66.67 ns. The effective sweep direction resulting from phase modulation was from low frequency to high frequency in the case of $^{119}$Sn, $^{195}$Pt, and $^{71}$Ga. $^2$H experiments were tested with both low-to-high frequency and high-to-low frequency sweep directions (*vide infra*).

## 2.3. Numerical optimizations of frequency-swept pulses

All OCTOBER pulses were generated with the open source software package SIMPSON (version 4.2) [56], using the Shared Hierarchical Academic Research Computing Network (SHARCNET). Three types of FS pulses (*i.e.*, WURST, THT, and HS) were used as starting points in the optimization procedures, with the starting parame-

ters listed above. The pulse lengths, the number of points in the pulses, and the maximum RF powers were varied for each pulse type and experiment. The exit tolerance on the target function was $10^{-6}$ and the exit tolerance during each line search was $10^{-3}$, with an initial step size of 10 for the bracketing minimum, and a maximum of 1000 iterations for the optimization [51]. Pulses were optimized for specific systems using combinations of CS and/

**Table 1**
Chemical shift and electric field gradient tensor parameters.

| Compound | Nucleus | Spin | $\delta_{iso}$ (ppm)[a] | $\Omega$ (ppm)[a] | $\kappa$[a] | $C_Q$ (MHz)[b] | $\eta_Q$ [b] | Ref. |
|---|---|---|---|---|---|---|---|---|
| SnO | $^{119}$Sn | 1/2 | −208 | 988 | 1 | – | – | 55 |
| Pt(NH$_3$)$_4$Cl$_2$·H$_2$O | $^{195}$Pt | 1/2 | −2540 | 7250 | −0.96 | – | – | 24 |
| α-glycine-$d_2$ | $^2$H | 1 | – | – | – | 0.170 | 0 | 57[c] |
| GaPcCl | $^{71}$Ga | 3/2 | 130 | – | – | 21.2 | 0.05 | 23 |

[a] The chemical shift (CS) tensor for each system is defined with principal components $\delta_{11} \geq \delta_{22} \geq \delta_{33}$, where $\delta_{iso} = \frac{1}{3}(\delta_{11} + \delta_{22} + \delta_{33})$, $\Omega = (\delta_{11} - \delta_{33})$, and $\kappa = 3(\delta_{22} - \delta_{iso})/\Omega$.
[b] The electric field gradient (EFG) tensor for each system is defined with principal components $|V_{33}| \geq |V_{22}| \geq |V_{11}|$, with $C_Q = eQV_{33}/h$ and $\eta_Q = (V_{11} - V_{22})/V_{33}$.
[c] We report tensor parameters for one site, although Müller *et al.* report two sites with different parameters using single-crystal NMR.
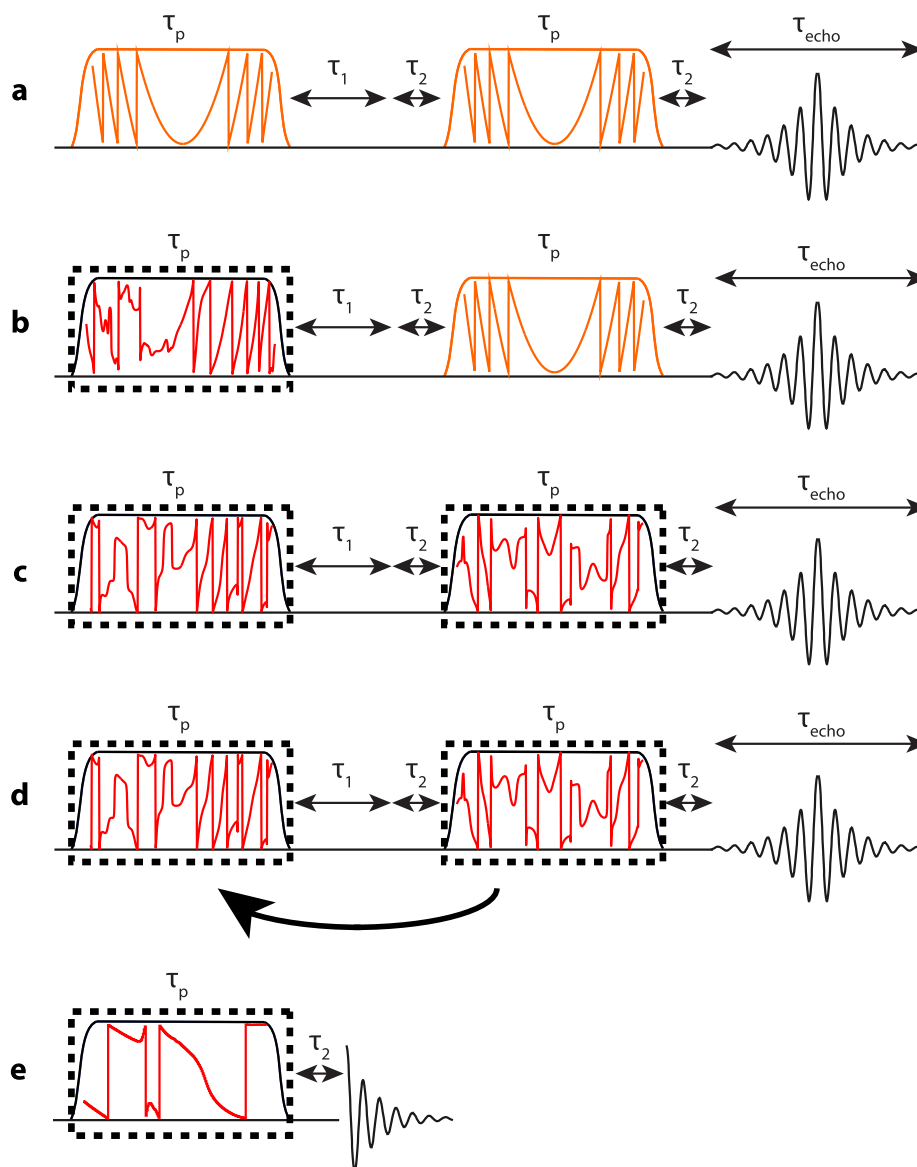


**Scheme 1.** (a) The WURST-echo sequence used as a starting point for optimizing the amplitudes and phases of the excitation and refocusing pulses with OCT. (b) The **Eopt** protocol, which features optimization of only the excitation pulse. (c) The **ERopt** protocol, which features simultaneous optimization of both the excitation and refocusing pulses. (d) The **REseq** protocol, which features the optimization of the refocusing pulse first, followed by sequential optimization of the excitation pulse. (e) A Bloch decay sequence in which the excitation pulse is optimized prior to the dead time.

**Table 2**
Properties of nuclei investigated in this work.

| Nucleus | Spin | Natural Abundance (%) | Gyromagnetic Ratio ($\times 10^7$ rad T$^{-1}$ s$^{-1}$) | Larmor Frequency at 9.4 T (MHz) | Quadrupole Moment (fm$^2$) |
|---|---|---|---|---|---|
| $^{119}$Sn | 1/2 | 8.59 | −10.0317 | 149.211 | – |
| $^{195}$Pt | 1/2 | 33.832 | 5.8383 | 86.015 | – |
| $^{2}$H | 1 | 0.0115 | 4.10662919 | 61.442 | 0.286 |
| $^{71}$Ga | 3/2 | 39.892 | 8.18117 | 122.026 | 10.7 |

or EFG tensor parameters obtained from previous studies (Table 1) [23,24,55,57]. Simulations made use of the Zaremba-Conroy-Wolfsberg (ZCW) powder averaging scheme with either 986, 4180, or 28,656 orientations. All OCTOBER pulses were tested for performance in numerical simulations using SIMSPON before being applied in experimental trials. All pulse sequences, OCTOBER pulse shapes, and SIMPSON input files used are available upon request.

### 2.4. Solid-State NMR spectroscopy

NMR spectra were acquired using a Bruker Avance III HD console and a 9.4 T Oxford wide-bore magnet at resonance frequencies of $\upsilon_0(^{119}\text{Sn}) = 149.211$ MHz, $\upsilon_0(^{195}\text{Pt}) = 86.015$ MHz, $\upsilon_0(^{2}\text{H}) = 61.422$ MHz, and $\upsilon_0(^{71}\text{Ga}) = 122.026$ MHz. A Varian/Chemagnetics 5 mm double resonance (HX) probe was used for $^{119}$Sn NMR experiments. A Revolution 5 mm double-resonance (HX) ultra-low-temperature (ULT) probe was used for $^{195}$Pt, $^{2}$H, and $^{71}$Ga

NMR experiments. All data were collected under static conditions (i.e., stationary samples). Spectra of compounds having protons were acquired with $^1$H continuous-wave (CW) decoupling with RF fields ranging between 40 and 50 kHz.

RF pulse powers and chemical-shift reference frequencies were calibrated for each nucleus using the following standards: (i) $^{119}$Sn reference: Sn(CH$_3$)$_4$ (l) with $\delta_{iso} = 0.0$ ppm; (ii) $^{195}$Pt reference: 1.0 M Na$_2$PtCl$_6$ (aq) with $\delta_{iso} = 0.0$ ppm; (iii) $^{2}$H reference: D$_2$O (l) with $\delta_{iso} = 4.8$ ppm; (iv) $^{71}$Ga reference: 1.0 M Ga(NO$_3$)$_3$ (aq) with $\delta_{iso} = 0.0$ ppm.

Spin-echo and CPMG-type spectra were processed using a Fourier transformation followed by magnitude calculation (resulting CPMG spectra therefore have a "spikelet" manifold appearance). Bloch-decay style spectra were processed using a Fourier transformation, a combination of zeroth and first order phasing, and a fifth-order polynomial baseline correction. The experimental conditions, acquisition parameters, and RF field strengths, used for each experiment are summarized in Tables S1–S10, ESI.

## 3. Results and discussion

### 3.1. Overview

In the sections that follow, first, using both simulation and experiment, HS and THT pulses were tested for each system, and the resulting spectra compared to those obtained with WURST pulses. Second, new OCTOBER pulses were generated using OCT, with WURST, THT, and HS pulses as starting functions; this was followed by experimental testing on each system [51]. Finally, the spin polarization was tracked during numerical simulations of the pulse sequences by monitoring the time evolution of the density matrix via the Liouville-von Neumann equation; this analysis is used to rationalize differences between simulated and/or experimental spectra, and to understand the mechanisms of the WURST, THT, HS, and new OCTOBER pulses. The mechanisms of WURST and OCTOBER pulses are further explored using their time-resolved Fourier transforms. All pulses were tested experimentally using either spin-echo or CPMG-type pulse sequences, with a select set of tests using Bloch decay sequences (vide infra) [5,9].

To create OCTOBER pulses, appropriate pulse parameters for each starting pulse (i.e., prior to optimization) were determined from numerical simulations using SIMPSON. Three distinct optimization protocols were developed for testing OCTOBER pulses in spin-echo pulse sequences (of the form $\pi/2 - \tau_1 - \tau_2 - \pi - \tau_2 -$ acquire, Scheme 1, where $\tau_2$ is the ring-down or dead-time delay, and $\tau_1 = (\tau_{echo} - \tau_p)/2$): (i) the excitation pulse is optimized from one of the starting functions, but the refocusing pulse is left unoptimized (**Eopt**); (ii) the excitation and refocusing pulses are optimized simultaneously (**ERopt**); (iii) the refocusing and excitation pulses are optimized sequentially (i.e., just the refocusing pulse is first optimized using the broadband refocusing protocol of Tosner [51], followed by a subsequent optimization of the excitation pulse, **REseq**). In the current work, the amplitudes and phases of the excitation and refocusing pulses are subjected to OCT routines for different sets of fixed pulse widths in spin echo sequences, for the purpose of maximizing signal; this is similar to the strategy
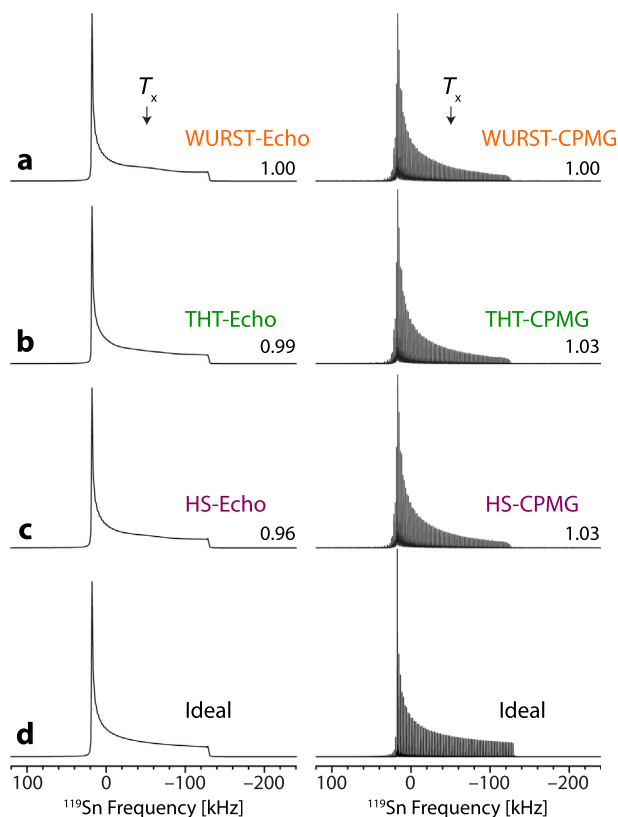


**Fig. 1.** Simulated (left) and experimental (right) $^{119}$Sn NMR spectra of SnO acquired using a spin-echo pulse sequence (a) with WURST pulses, (b) THT pulses, and (c) HS pulses. (d) Simulations of ideal patterns generated using rectangular pulses of infinite power (left Hahn-echo; right CPMG). The transmitter offset frequency is set to ca. −54 kHz (i.e., −54 kHz with respect to $\upsilon_0(^{119}\text{Sn})$) for acquisition of all $^{119}$Sn spectra (the transmitter position is indicated by $T_x$ in the diagram). Pulses used to acquire these spectra had values of $\tau_p = 25$ μs and $N_p = 375$ points. Relative simulated and experimental integrated intensities are shown, normalized with respect to the spectra acquired with the WURST-echo and WURST-CPMG sequences, respectively.
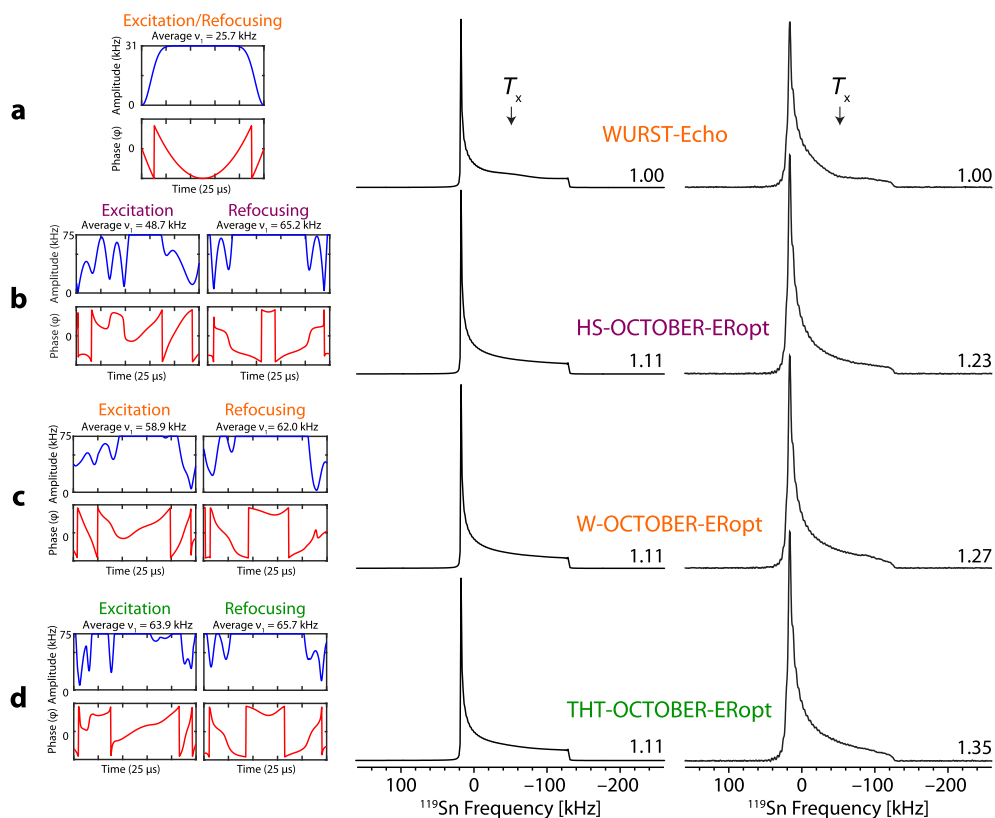
**Fig. 2.** RF amplitude and phase modulation profiles (left column) and simulated (middle column) and experimental (right column) $^{119}$Sn NMR spectra of SnO for the pulse sequences utilizing the following pulses: (a) WURST, (b) HS-OCTOBER-**ERopt**, (c) W-OCTOBER-**ERopt**, and (d) THT-OCTOBER-**ERopt**. Relative simulated and experimental integrated intensities are shown, normalized to the spectrum acquired with the WURST-echo sequence.
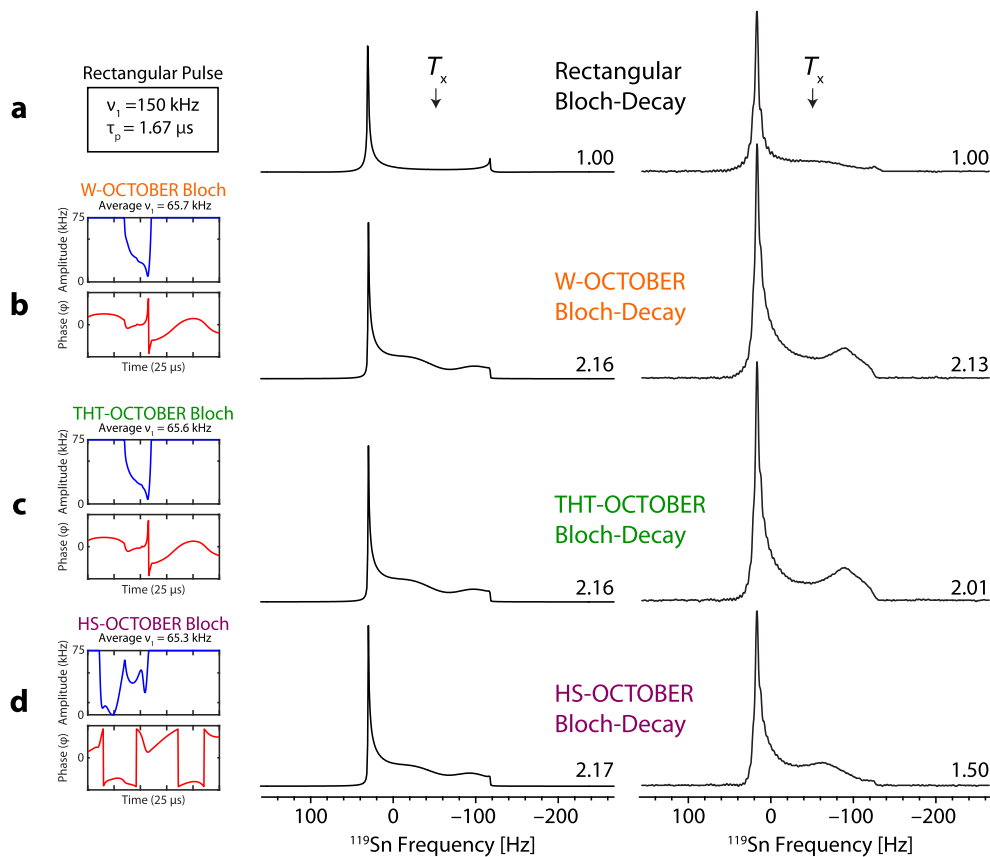


**Fig. 3.** RF amplitude and phase modulation profiles (left column) for OCTOBER pulses and $^{119}$Sn NMR spectra of SnO (simulated in the middle column, experimental in the right column) for Bloch-decay style pulse sequences using OCTOBER pulses optimized from (a) WURST, (b) THT, and (c) HS pulses. Relative simulated and experimental integrated intensities are shown, normalized to the spectrum acquired with the rectangular-pulse Bloch-decay sequence.

proposed by Kallies and Glaser, who went further in carefully examining the interdependence of these parameters on pulse widths and interpulse delays [49]. In addition, OCTOBER pulses were designed and optimized for use in single-pulse Bloch decay experiments ($\pi/2 - \tau_2 - acq$). When Bloch decay experiments are conducted upon systems with inhomogeneously broadened patterns, the FID can undergo a substantial decay during the dead time, resulting in signal loss and severe distortions (this is why Bloch decay experiments are rarely used for such systems). Hence, the new OCTOBER pulses that are designed for Bloch decay experiments account for the evolution of spin polarization during both the excitation pulse and the dead time, with the hope that coherent spin polarization can survive through to the acquisition period (this is akin to the design of ICEBERG pulses by Glaser and coworkers) [44].

OCTOBER pulses were created from numerous permutations of the above-mentioned optimization methods, starting pulses, and pulse parameters. For each system studied in this work, at least 100 pulses were optimized and tested in numerical simulation (i.e., by varying the selection of the three classes of starting pulses, four optimization methods, three sets of starting pulse parameters, and three or four starting RF amplitudes). Select examples of the best performing OCTOBER pulses are shown, as well as some underperforming cases (i.e., those that produce results that disagree with their simulated counterparts) for comparison.

Several metrics are used to assess the performance of these pulses and their implementation in spin-echo type sequences: (i) the *integrated signal intensity* under the powder pattern is calculated in both simulation and experiment and is normalized with respect to spectra obtained using WURST pulses (unless otherwise stated); (ii) the *uniformity* of the powder pattern is assessed by qualitative comparison to an ideal simulated pattern; and (iii) the *average RF amplitude* used throughout the duration of a pulse. In all cases, maximum integrated signal intensity, high uniformity, and low average RF amplitudes are desirable. OCTOBER pulses are optimized with a set maximum RF amplitude; however, the amplitudes of the optimized pulses do not remain at the maximum for the entire duration of the pulse in most cases (*vide infra*).

Four systems, which differ in terms of the types of nuclei, receptivities, and respective NMR interactions (Table 2) [58,59], were selected for this study, based on previous reports. These include SnO for $^{119}$Sn ($I = 1/2$) [55], Pt(NH$_3$)$_4$Cl$_2$·H$_2$O for $^{195}$Pt ($I = 1/2$) [24], $\alpha$-glycine-$d_2$ for $^2$H ($I = 1$) [60], and gallium phthalocyanine chloride (GaPcCl) for $^{71}$Ga ($I = 3/2$) [23,61]. All feature spectra with broad patterns with breadths ranging from *ca.* 160 to 630 kHz at 9.4 T (a description of the rationale for choosing each of these systems is given in the ESI). The two quadrupolar nuclei, $^2$H and $^{71}$Ga, are of particular interest, since they present the opportunity to study the influences of the general FS pulses and OCTOBER pulses on overlapping patterns arising from satellite transitions (STs, 0
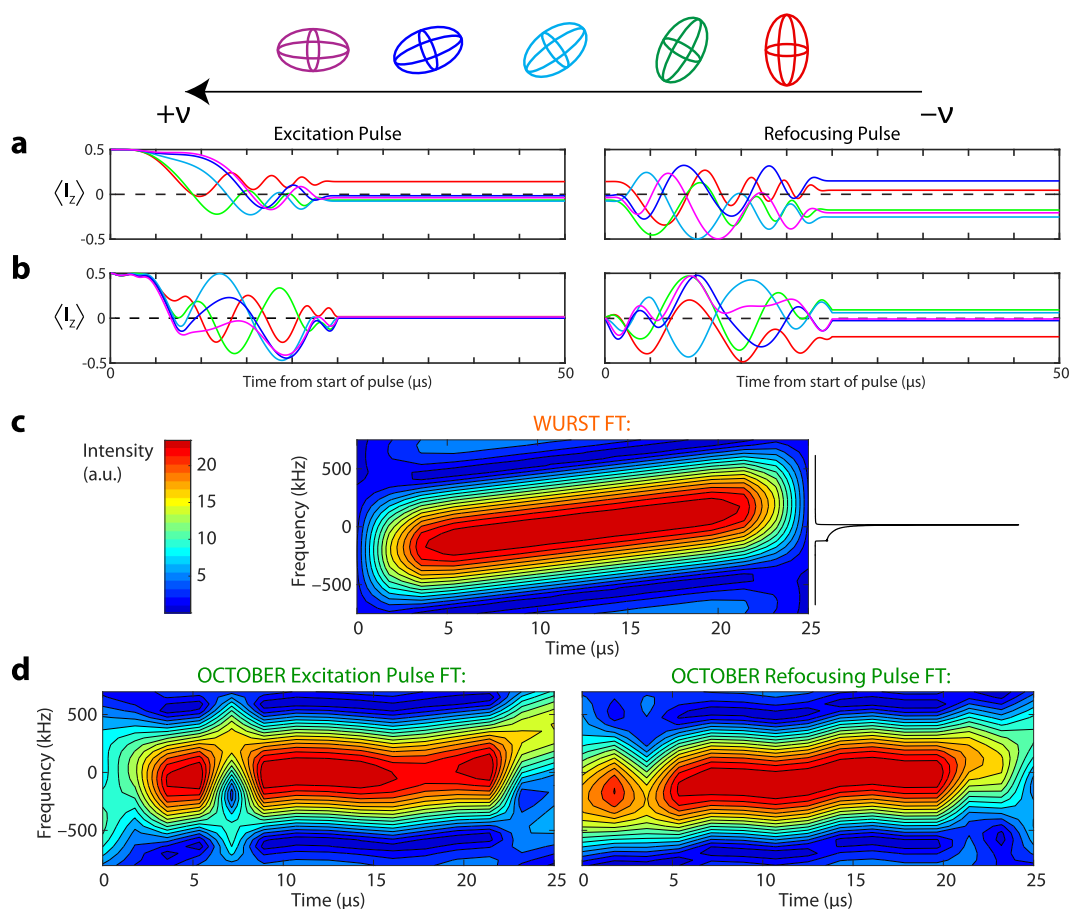


**Fig. 4.** Plots of the evolution of the expectation value of the z-component of the spin polarization, $\langle I_z \rangle$ for five crystallite tensor orientations ($\beta = 90°$ (purple), 70° (navy), 54.745° (cyan), 30° (green), and 0° (red), pictured at the top of the figure). The plots are shown (a) during a spin-echo pulse sequence utilizing WURST pulses (sweeping in a low- to high-frequency direction), and (b) during a spin-echo pulse sequence utilizing THT-OCTOBER-**ERopt** pulses. Time-resolved Fourier transforms of (c) WURST and (d) THT-OCTOBER-**ERopt** pulses. All pulse parameters are described in Fig. 2. See videos in the **ESI** for Bloch Sphere projections of spin polarization. (For interpretation of the references to colour in this figure legend, the reader is referred to the web version of this article.)

↔ ±1) or the central transition (CT, +1/2 ↔ −1/2) and STs (±3/2 ↔ ±1/2), respectively. Currently, it is not possible to acquire uniformly excited, distortion-free spectra for these systems using high-power rectangular pulses in Bloch-decay, Hahn-Echo, or CPMG-type pulse sequences on probes with 5 mm i.d. coils at 9.4 T.

### 3.2. $^{119}$Sn NMR simulations and experiments

#### 3.2.1. Simulation and implementation of frequency-swept pulses

The optimal pulse parameters and RF amplitudes were determined by numerical simulations of the $^{119}$Sn NMR powder pattern of SnO (breadth of 160 kHz at 9.4 T), in the context of spin-echo pulse sequences (Fig. 1). From analysis of the signal intensities and pattern uniformities of the simulated spectra (*vide supra*), the best pulse widths, numbers of points, and approximate RF amplitudes that led to the "best" simulated spectra (as judged by comparison to an "ideal" spectrum simulated with infinite power and excitation bandwidth) were used in experiments (Fig. S1).

The three FS pulses were implemented in a CPMG-type pulse sequence to acquire experimental $^{119}$Sn SSNMR spectra of SnO (Fig. 1). Experimental RF amplitudes were arrayed to find the best performance for each of these pulse shapes for a given pulse length and sweep range (see Tables S1–S10). WURST pulses required 31.3 kHz of maximum RF amplitude for best performance, whereas THT and HS required 31.3 kHz and 62.7 kHz of maximum RF amplitude, respectively. The higher power requirements of HS over the WURST pulse may seem like a problem for general implementation of these pulses; however, the maximum RF amplitude for the HS pulse occurs for only a small duration of the pulse period (*i.e.*, the HS pulses use only *ca.* 49% of the maximum RF amplitude on average whereas WURST and THT pulses use *ca.* 82% and 93% of the maximum RF amplitude, respectively). The patterns are uniformly excited, and match fairly well with the ideal CPMG pattern in terms of uniformity (*N.B.*: the patterns are dominated by the effects of CSA, which is the only interaction modeled in the simulations; the influences of $^{119}$Sn-$^{119}$Sn and $^{119}$Sn-$^{117}$Sn dipolar- and *J*-couplings are visible at the outer discontinuities, of the experimental spectra, see also Fig. S2) [62]. The WURST-CPMG pattern is consistent with previously reported spectra [55]. These results demonstrate that THT and HS pulses are capable of broadband excitation and refocusing in a CPMG-type sequence.

#### 3.2.2. Performance of OCTOBER pulses

$^{119}$Sn SSNMR spectra were simulated and acquired experimentally using a spin-echo sequence featuring OCTOBER pulses optimized from WURST, THT, or HS pulses as starting points (Fig. 2). The left column shows the optimized amplitude and phase profiles of the pulses, while the middle and right columns display the corresponding simulated and experimental spectra. OCTOBER pulses were optimized using the three aforementioned protocols (*i.e.,* **Eopt**, **ERopt**, and **REseq**, *vide supra*). Each of the spectra in Fig. 2 (and throughout the remainder of the paper) are denoted by a code that describes both the starting pulse shape and optimization protocol. For instance, the code HS-OCTOBER-**ERopt** denotes a spectrum acquired with OCTOBER pulses that are generated with an HS pulse as a starting point, with simultaneous optimization of the excitation and refocusing pulses (**ERopt** protocol). OCTOBER pulses suitable for experimental implementation were chosen based on comparison of numerically simulated powder patterns obtained using ideal pulses and OCTOBER pulses (Fig. S3). The best performances of the pulse sequences are gauged against the simulated and experimental spectra obtained from the WURST-echo pulse sequence (normalized total integrated intensities of 1.0 are assigned to these spectra, since WURST pulses are a current standard method for acquiring broad powder patterns *via* direct excitation of the target nucleus) [1].

The simulated spectra in all four cases have uniformly excited patterns with OCTOBER-echo spectra showing enhancements of *ca.* 11% in each case. The experimental patterns obtained with HS-OCTOBER-**ERopt**, W-OCTOBER-**ERopt,** and THT-OCTOBER-**ERopt** sequences are representative of some of the best results of all trials. A larger array of different OCTOBER pulses tested is available in Fig. S4. The integrated intensities of the OCTOBER spectra exceed that of the WURST spectrum by as much as *ca.* 35%. Numerical simulations suggest that only an 11% gain in signal is achievable by a WURST-echo sequence in comparison to an idealized spin-echo experiment (Fig. S3); therefore, it is likely that the spectra obtained with the OCTOBER-echo sequences are representative of the maximum amount of observable signal by direct excitation for this spin system.

The phase and amplitude modulations of the pulses (Fig. 2, left column) display a substantial amount of variation, with the different starting pulses leading to unique solutions in each case. All of the sequences feature OCTOBER pulses requiring substantially higher maximum RF values than the $\nu_1 = 31$ kHz used in the WURST-echo pulse sequence. This RF amplitude required for the WURST pulse was experimentally optimized and represents the best performance possible when using that pulse shape for this powder pattern (*i.e.*, if the resulting higher RF amplitudes are used with the same WURST pulse parameters, the signal intensity and pattern uniformity are observed to decrease). All of the OCTOBER pulses used require a maximum $\nu_1 = 75$ kHz, but the average RF
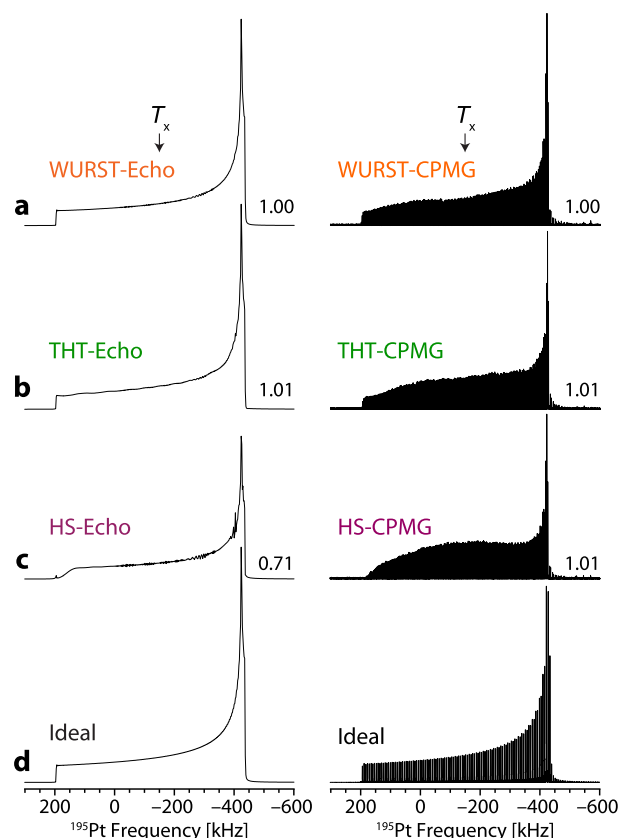


**Fig. 5.** Simulated (left) and experimental (right) $^{195}$Pt NMR spectra of Pt(NH$_3$)$_4$-Cl$_2$·H$_2$O acquired using a spin-echo pulse sequence (a) with WURST pulses, (b) THT pulses, and (c) HS pulses. (d) Ideal patterns generated using rectangular pulses of infinite power (left, Hahn-echo; right, CPMG). The transmitter offset frequency, indicated by $T_x$, is set to *ca.* −150 kHz (*i.e.*, −150 kHz with respect to $\nu_0(^{195}$Pt)) for acquisition of all spectra. Pulses used to acquire these spectra had values of $\tau_p = 40$ μs and $N_p = 600$. Relative simulated and experimental integrated intensities are shown, normalized with respect to the spectra acquired with the WURST-echo and WURST-CPMG sequences, respectively.

amplitude varies between 48.7 and 65.7 kHz. In some cases, trends can be distinguished among these unique solutions. For example, all three OCTOBER refocusing pulses take on symmetrical amplitude and phase modulations, and could therefore represent a general optimized refocusing waveform. Similar modulations were observed by Kobzar and coworkers for broadband refocusing pulses (BURBOP) [46]. The phase modulations indicate some degree of linear effective frequency sweep behaviour, though parts of the phase functions are non-quadratic, as indicated by deviation from a parabolic line shape (*vide infra*).

OCTOBER pulses were also tested in a preliminary set of Bloch-decay style experiments (Fig. 3). For these experiments, $\tau_2 = 6$ μs was found to be an optimal delay time for OCTOBER pulses after theoretically and experimentally arraying this parameter. Simulations predict that OCTOBER pulses generate some distortions in the powder pattern, but increase the detectable signal by a factor of up to *ca*. 2.17, and have increased excitation bandwidth in comparison to high-power rectangular pulses; corresponding experimental spectra display similar features, though the agreement is not exact (with an increased signal intensity factor as high as *ca*. 2.13). WURST- and THT-OCTOBER Bloch decay pulses are very similar, both in terms of amplitude and phase modulation, and could therefore represent an optimum pulse shape (or potential pathway to an optimum shape) for the particular maximum RF amplitude applied in these two cases. We note that O'Dell et al. have previously used OCT to generate pulses to excite the $^{119}$Sn SSNMR pattern of SnO in Bloch decay experiments [55]. In that work, the starting functions of the pulses were generated randomly; as a result, we are unable to reproduce the identical optimized pulse shapes from that work. In the current work, the starting pulse amplitudes and phases lead to the same unique solutions for each

protocol every time. *N.B.*: The use of OCTOBER pulses in Bloch-decay sequences is only tested for the $^{119}$Sn system in the current work; further investigations on other systems are ongoing.

### 3.2.3. Spin dynamics

The spin dynamics under the influences of WURST and OCTOBER pulses were studied for this system. With SIMPSON, it is possible to track the time evolution of the density matrix for a spin system throughout a pulse sequence [56]. Using the density matrix, the expectation value for any operator can be calculated. The expectation value for $\mathbf{I}_z$, $\langle \mathbf{I}_z \rangle$, for a spin-1/2 nucleus, was calculated in several simulations from

$$\langle \mathbf{I}_z \rangle = \mathrm{Tr}\{\rho \mathbf{I}_z\} = (\rho_{11} - \rho_{22})/2 \qquad (3.1)$$

and used to track the *z*-projection of the spin polarization during the pulses in spin-echo sequences for key tensor orientations (Fig. 4). The tensor orientations under consideration are described by the orientation of the magnetic field, $\mathbf{B}_0$, with respect to the highest-frequency component of the chemical shift tensor, $\delta_{33}$, as defined by the angle β (*i.e.*, if β = 0°, $\mathbf{B}_0$ and $\delta_{33}$ are coincident; if β = 90°, they are perpendicular (cf. Fig. S5a)). For simplicity, the CS tensor is assumed to be axially symmetric (*i.e.*, the value of the azimuthal angle, α, is irrelevant), and five key orientations are chosen such that they are distributed more or less evenly across the pattern (*i.e.*, β = 90°, 70°, 54.74°, 30°, and 0°); hereafter, we refer to these as *crystallite tensor orientations* for brevity and clarity).

To start, it is instructive to consider the behaviour of spin polarization during a WURST-echo pulse sequence for different crystallite tensor orientations (Fig. 4a). The excitation pulse effectively generates transverse spin polarization (*i.e.*, $\langle \mathbf{I}_z \rangle = 0$) for all but the β = 0° crystallite tensor orientation. The subsequent refocusing
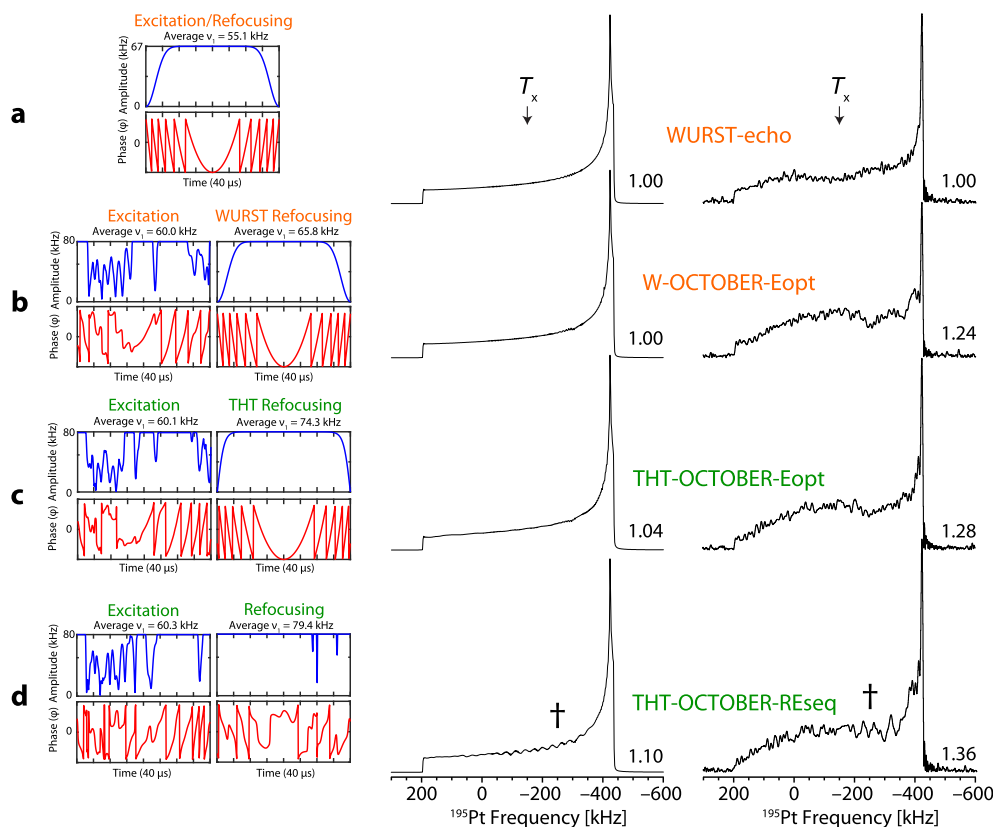


**Fig. 6.** RF amplitude and phase modulation profiles (left column) and simulated (middle column) and experimental (right column) $^{195}$Pt NMR spectra of Pt(NH$_3$)$_4$Cl$_2$·H$_2$O for the pulse sequences utilizing the following pulses: (a) WURST, (b) W-OCTOBER-**Eopt**, (c) THT-OCTOBER-**Eopt**, and (d) THT-OCTOBER-**REseq**. Relative simulated and experimental integrated intensities are shown, normalized with respect to the spectrum acquired with the WURST-echo sequence. Spectral distortions are denoted by †.

pulse does not result in the return of all of the spin polarization into the $xy$-plane, as evidenced by substantial non-zero values of $\langle \mathbf{I}_z \rangle$ for each crystallite.

For comparison, use of the THT-OCTOBER-**ERopt** pulses in a spin-echo sequence was studied, since this sequence produces a pattern with increased signal enhancement relative to the analogous WURST-echo sequence (*cf.* Fig. 2d). The use of THT-OCTOBER-**ERopt** pulse for excitation results in $\langle \mathbf{I}_z \rangle = 0$ for all crystallite orientations, and the subsequent refocusing pulse returns spin polarization in the transverse plane more effectively than that in the WURST-echo sequence discussed above (*i.e.*, all $\langle \mathbf{I}_z \rangle$ values are closer to zero, for all but the $\beta = 0°$ orientation). Therefore, the resulting signal enhancement in comparison to the WURST-echo experiment clearly results from increased spin polarization in the transverse plane. Bloch spheres [63] can be used to visualize the evolution of the $x$-, $y$-, and $z$-components of spin polarization during the pulses, as illustrated in videos included in the ESI.

In order to further understand the mechanisms of these pulses, time-resolved Fourier transforms are utilized in a manner similar to those presented in work by O'Dell et al. [53,54]. The time-resolved Fourier transform of a WURST pulse, with time on the $x$-axis, frequency on the $y$-axis, and pulse amplitude expressed in units of arbitrary intensity on the $z$-axis, is shown for the case of the SnO pattern (Fig. 4c). A uniform effective frequency sweep is apparent as the offset frequency changes as a function of time, as indicated by the amplitude modulation of the pulse. For the THT-OCTOBER-**ERopt** excitation pulse, there is not a uniform effective

frequency sweep over the pulse duration (Fig. 4d); rather there are three distinct features to note: (i) There is a gap in intensity around 7 µs, corresponding to the dip in the amplitude modulation of the pulse; (ii) from 0 to 15 µs, the effective frequency offset does not change; (iii) from 15 to 20 µs, the offset moves in a high-frequency direction. For the refocusing pulse, there is a prevalent frequency sweep between 10 and 15 µs. This analysis suggests that these OCTOBER pulses have characteristics of both frequency-swept pulses (with some degree of linearity) and rectangular pulses with homogenous excitation bandwidths.

### 3.3. $^{195}$Pt NMR simulations and experiments

#### 3.3.1. Simulation and implementation of frequency-swept pulses

Optimal parameters for WURST, THT, and HS pulses were determined using numerical simulations of the $^{195}$Pt NMR powder pattern of $Pt(NH_3)_4Cl_2 \cdot H_2O$ (Fig. 5, left column). Simulations indicate that the WURST and THT pulses are capable of broadband excitation and refocusing; however, the HS pulses provide a limited excitation bandwidth, as indicated by reduced intensity in the high frequency side of the pattern (this holds for a variety of different combinations of possible HS parameters). *N.B.:* Because the sweep width in the phase modulation of the HS pulse is controlled by a combination of parameters µ and β (see ESI, Equations S1.7 through S1.9), it is challenging to parametrize this pulse for larger excitation and refocusing bandwidths.
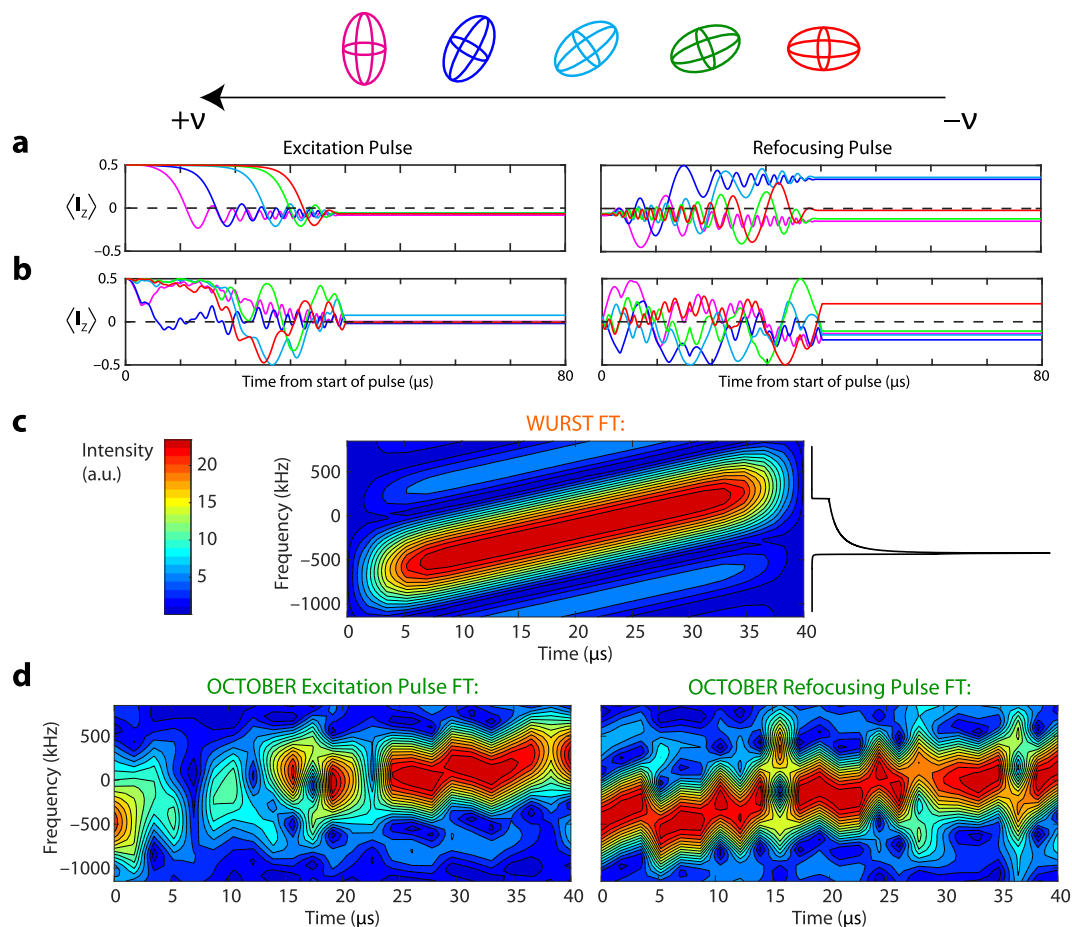


**Fig. 7.** Evolution of the expectation value of the $z$-component of the spin polarization for crystallite tensor orientations ($\beta = 0°$ (purple), 30° (navy), 54.745° (cyan), 70° (green), and 90° (red), pictured at the top of the figure) (a) during a spin-echo pulse sequence utilizing WURST pulses (sweeping in a low- to high-frequency direction), and (b) during a spin-echo pulse sequence utilizing THT-OCTOBER-**REseq** pulses. Time-resolved Fourier transforms of (c) WURST and (d) THT-OCTOBER-**REseq** pulses. All pulse parameters are described in Fig. 6. (For interpretation of the references to colour in this figure legend, the reader is referred to the web version of this article.)

The performance of the three FS pulses are demonstrated experimentally in the context of CPMG-type experiments (Fig. 5, right column). WURST and THT pulses yield patterns of uniform appearance, and compare favorably with the ideal simulated pattern and previously obtained spectra [24]. HS pulses underperform slightly in terms of the powder pattern uniformity, in agreement with simulations, again due to the limited excitation bandwidth. The results from these and the $^{119}$Sn NMR experiments above suggest that HS pulses may not be as effective as WURST or THT pulses for the acquisition of broad SSNMR patterns for spin-1/2 systems.

### 3.3.2. Performance of OCTOBER pulses

OCTOBER pulses were first tested with numerical simulations (Fig. 6). W-OCTOBER-**Eopt** and THT-OCTOBER-**Eopt** spectra show uniform pattern excitation, and compare well to the ideal pattern, with minor spectral distortions. The THT-OCTOBER-**REseq** pattern is comparable to the ideal pattern; however, some oscillations are present in the vicinity of crystallites corresponding to crystallite tensor orientations with β near the magic angle (indicated by †).

These OCTOBER pulses were implemented in spin-echo experiments (Fig. 6). WURST-OCTOBER-**Eopt** and THT-OCTOBER-**Eopt** variants provide relatively uniform excitation of the pattern (some distortions are observed near the centres of gravity of the patterns), but with enhanced signal intensities relative to the pattern acquired with the WURST-echo sequence. The powder pattern acquired using THT-OCTOBER-**REseq** pulses has noticeable dips near the magic-angle crystallite tensor orientation (indicated by †). A possible reason for these spectral distortions is the limiting maximum RF amplitude in the refocusing pulses (i.e., in Fig. 6d, the pulse amplitude of the refocusing pulse is almost always at a maximum). Even though this is a limitation in this particular example, the optimized pulse shape may be instructive for the purposes of improved parameterization. For instance, setting a higher maximum RF amplitude in the optimization protocol may resolve these powder pattern distortions (vide infra); however, higher RF amplitudes are often difficult to achieve for nuclei with low to moderate gyromagnetic ratios such as $^{195}$Pt. As in the case of the $^{119}$Sn OCTOBER simulations and experiments, the average RF requirement of the excitation pulses is lower than the maximum allowed RF, making the power requirements of these new OCTOBER pulses comparable to the those of analogous WURST pulses. A larger array of tests of different OCTOBER pulses is shown in Fig. S6. Improved performance of the optimized refocusing pulse may also result from the use of longer pulses. The uses of increased RF amplitudes and longer pulses for improved performance of broadband refocusing pulses has previously been suggested by Kobzar and coworkers [41]. Future studies of such OCTOBER pulses must examine the use of both higher RF amplitudes (where possible) and pulse widths that are significantly larger than the maximum of 40 μs used in the current work.

### 3.3.3. Spin dynamics

The spin dynamics were also examined for WURST and OCTOBER pulses used in $^{195}$Pt NMR simulations and experiments. The plots in Fig. 7a show the z-component of spin polarization for both the excitation and refocusing WURST pulses. The excitation pulse brings all of the polarization near to the xy-plane; however, the refocusing pulse only effectively retains the polarization associated with the β = 90° orientation near the xy-plane. For the THT-OCTOBER-**REseq** pulses in a spin-echo pulse sequence (Fig. 7b), the excitation pulse brings most of the spin polarization into the xy-plane after some degree of rapid oscillatory behaviour. The refocusing pulse places a higher degree of spin polarization near the xy-plane than the WURST-echo sequence, resulting in a net increase of transverse spin polarization; however, the spin polarization of the β = 90° crystallite tensor orientation is not refocused

effectively. Again, this explains the improvement in signal intensity for the resulting pattern from these pulses in simulation and experiment; however, while this amount of signal enhancement approaches the theoretical maximum by direct excitation, there is still room for improvement in terms of both signal intensity and the creation of distortionless patterns.

Time-resolved Fourier transforms of the pulses are again used to analyze these pulse shapes. The large sweep width parameterization necessary for this system (ca. 1.2 MHz) is showcased in the FT of the WURST pulse (Fig. 7c). The THT-OCTOBER-**REseq** excitation pulse (Fig. 7d) appears to briefly excite disparate regions of the powder pattern for the first half of the pulse. In the latter half of the pulse, sweeping behaviour is observed primarily in the high frequency region of the pattern, but also changes sweep direction four times. The refocusing pulse continues this rapidly changing frequency-sweep direction behaviour, but the net frequency sweep bandwidth covers a much broader region. This fast switching of frequency sweep direction might be an important consideration when designing general pulse shapes for the acquisition of broad spin-1/2 patterns (vide infra).

### 3.4. $^2$H NMR simulations and experiments

#### 3.4.1. Implementation of frequency-swept pulses

To this point, only spin-1/2 nuclei have been considered, which involve one fundamental transition between nuclear spin states. $^2$H is a spin-1 nucleus, and therefore, there are two fundamental transitions. Furthermore, the powder patterns corresponding to
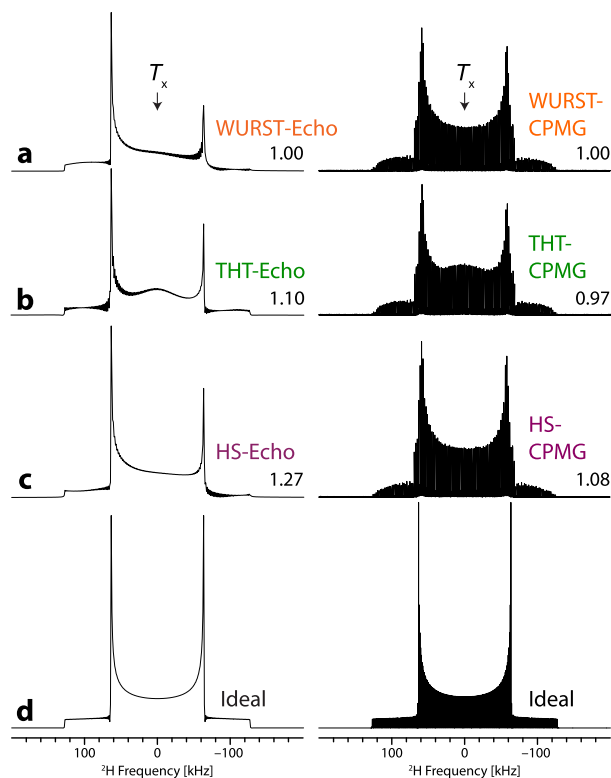


**Fig. 8.** Simulated (left) and experimental (right) $^2$H NMR spectra of α-glycine-$d_2$ acquired using a spin-echo pulse sequence (a) with WURST pulses, (b) THT pulses, and (c) HS pulses, which all sweep from low- to high-frequency. (d) Ideal patterns generated using rectangular pulses of infinite power (left Hahn-echo; right CPMG). The transmitter offset frequency is set to ca. 0 Hz (i.e., 0 Hz with respect to $\nu_0(^2H)$) for acquisition of all $^2$H spectra. Pulses used to acquire these spectra had values of $\tau_p = 25$ μs and $N_p = 375$. Relative experimental integrated intensities are shown, normalized with respect to the spectrum acquired with the WURST-CPMG sequence.

each transition overlap for certain crystallite tensor orientations, giving rise to two unique possibilities: (i) it is possible to polarize both transitions simultaneously, and (ii) there is the potential for the generation of multiple quantum coherences (MQCs). These factors can result in population transfers among spin states (*vide infra*) and must be taken into consideration when using FS pulses or designing new pulses with OCT. In particular, numerical simulations must use the full spin-1 density operator.

Numerical simulations of the $^2$H SSNMR pattern of α-glycine-$d_2$ using WURST, THT, and HS spin-echo pulse sequences are shown in Fig. 8 (left column). Simulations indicate that WURST and HS pulses appear to outperform THT pulses in terms of generating improved signal intensity. All three simulated spectra display a "lopsided" appearance, where the signal intensity on the high-frequency (left) side of the pattern is greater than on the low-frequency (right) side. This is a consequence of utilizing FS pulses that have specific sweep directions; in this case, the pulse sweep direction is from low- to high-frequency, which results in enhancement of the high-frequency portion of the powder pattern (a sweep in the opposite direction results in enhancement of the low-frequency portion of the pattern). This enhancement results from the DEISM (direct enhancement of integer spin magnetization) effect, which involves transfer of spin polarization between the +1, 0, and –1 spin states during the frequency sweep, resulting in enhancement of the signal in the high-frequency portion of the pattern in this case [64]. It is possible that DEISM effects may have practical applications for rapidly acquiring NMR spectra of integer spin systems [64,65].

WURST, THT, and HS pulses were used in a CPMG sequence to acquire experimental spectra (Fig. 8, right column). WURST and

HS pulses appear to outperform THT pulses, as predicted by numerical simulations; but interestingly, HS pulses provide slightly more signal enhancement than WURST pulses. This is likely because the effective frequency sweep rate of the HS pulse used is faster than that of WURST, which necessitates a higher RF amplitude. The combination of a faster sweep rate and higher RF amplitude has been shown to yield more signal intensity when using FS pulses [66]. HS pulses are effective for population transfer in experiments on half-integer quadrupolar nuclei [32]; however, they have not been used previously for both excitation and refocusing pulses, or for acquiring UWNMR patterns of integer spin nuclei.

### 3.4.2. Performance of OCTOBER pulses

OCTOBER pulses were generated using the three FS pulses as initial functions. The resulting simulated powder patterns (Fig. 9, middle column) show signal enhancements in comparison to the simulated WURST-echo spectrum. The effects of DEISM are still apparent in most of the spectra acquired using OCTOBER pulses. The HS-OCTOBER-**Eopt** pulses (Fig. 9, middle column) yield spectra with the expected DEISM effect; however, the W-OCTOBER-**ERopt** spectrum displays some unusual distortions, and does not take on the typical lopsided appearance associated with the DEISM effect.

These OCTOBER pulses were tested experimentally in spin-echo pulse sequences (Fig. 9, right column). Spectra acquired with the HS-OCTOBER-**Eopt** pulses have significantly higher signal intensity in comparison to the spectrum acquired with the WURST-echo sequence (*i.e.*, a factor of between *ca.* 2.11 to 2.43 times), in contrast to the modest gains predicted by simulations. It is important to note that the WURST pulses were executed with an
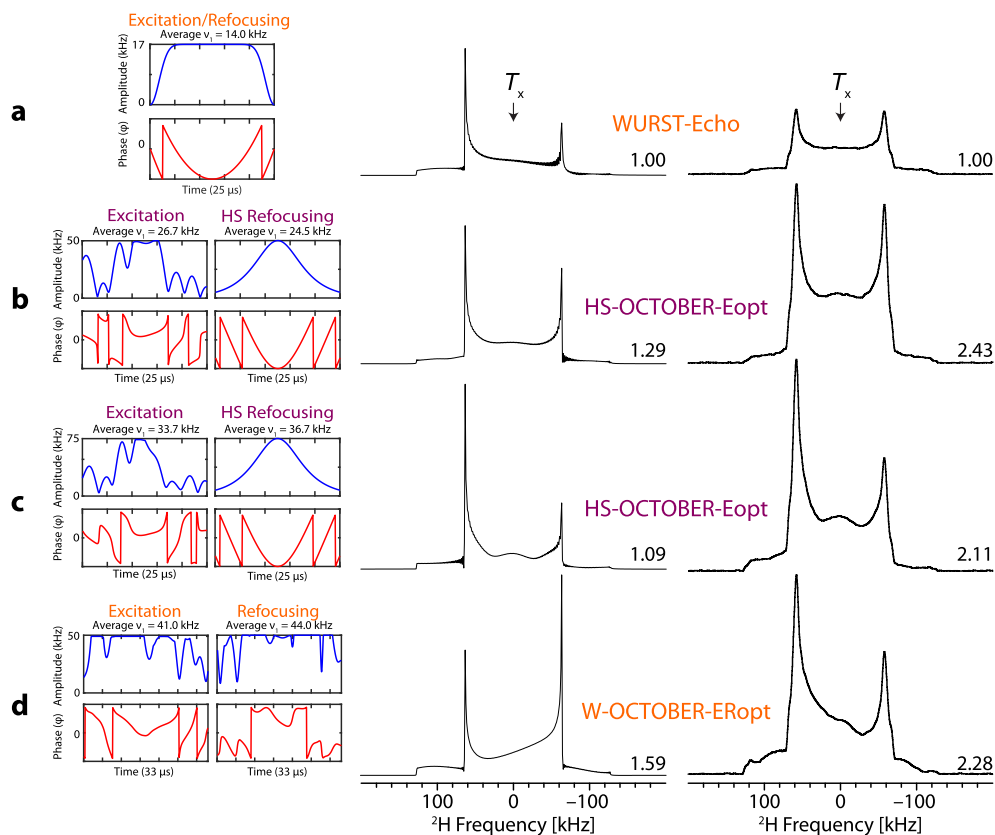


**Fig. 9.** RF amplitude and phase modulation profiles (left column) and simulated (middle column) and experimental (right column) $^2$H NMR spectra of α-glycine-$d_2$ (simulated in the middle, experimental to the right) for the pulse sequences utilizing the following pulses: (a) WURST, (b) HS-OCTOBER-**Eopt**, (c) HS-OCTOBER-**Eopt**, and (d) W-OCTOBER-**ERopt**. Relative simulated and experimental integrated intensities are shown, normalized with respect to the spectrum acquired with the WURST-echo sequence.

experimentally optimized RF amplitude; as in the case of the spin-1/2 systems discussed above, the arbitrary use of higher RF amplitudes with the same set of WURST pulse parameters results in lower signal intensity and an increased number of distortions. The best performance in terms of signal enhancement and uniform excitation is observed for the experiment using the HS-OCTOBER-**Eopt** pulse with a maximum RF amplitude of 50 kHz (an average of 24.5 kHz results from the optimization); the effects of DEISM are present, though not to the degree predicted by simulations (Fig. 9b). Using the same pulse optimization and sequence with a maximum RF amplitude of 75 kHz (average of 36.7 kHz) results in a spectrum that has lower overall signal intensity and augmented DEISM effects (Fig. 9c). The HS-OCTOBER-**Eopt** echo outperforms the WURST-echo experiment, with comparable power usage on the excitation pulses. Numerous other pulses were optimized and tested experimentally (Fig. S7); however, none matched the overall performance of sequences employing the HS-OCTOBER-**Eopt** pulse. The effects of DEISM are clearly present in the spectrum acquired with W-OCTOBER-**ERopt** pulses, with the high-frequency side of the pattern showing substantial signal enhancement (Fig. 9d); however, this spectrum does not match well with its simulated counterpart, featuring numerous distortions.

Consideration of the different types of OCTOBER pulses and how they are implemented in echo sequences may be instructive for how to better parameterize WURST or other FS pulses for a specific spin system. For example, the OCTOBER excitation pulses here appear to feature larger sweep widths (as indicated by additional wrapping points in the phase modulation), which would result in faster sweep rates; therefore, faster sweep rates may be required to effectively acquire broad $^2$H powder patterns. These pulses may also provide a superior alternative for the general use in population transfer for quadrupolar nuclei (Fig. S8).

### 3.4.3. Spin dynamics

Monitoring the spin dynamics under the influence of FS and OCTOBER pulses is crucial for understanding their performances. Methods for tracking the spin dynamics for an integer spin system are currently being investigated in a separate set of projects in our research group, and further discussion is beyond the scope of the current work. One reason for the complexity of this analysis is the presence of overlapping SQ transitions and simultaneous involvement of both single- and double-quantum transitions; both may play a very important role in population transfer and signal enhancement. The methods used to track spin dynamics in the current work are focused upon two-level systems and are more appropriate for studying spin-1/2 nuclei, including broad CT spectra of half-integer quadrupolar nuclei that have underlying ST patterns (*vide infra*) [63].

### 3.5. $^{71}$Ga simulations and NMR experiments

#### 3.5.1. Simulation and implementation of frequency-swept pulses

In numerical simulations of the $^{71}$Ga pattern of GaPcCl (Fig. 10, left column), the signal was detected using the $\mathbf{I}_{CT}$ operator, which involves only the $+1/2 \longleftrightarrow -1/2$ central transition (CT); however, the SIMPSON simulation still utilizes the full $I = 3/2$ density operator. This restriction on detection is necessary as the powder patterns for the satellite transitions (ST) are predicted to be over 21 MHz in breadth, which would require drastic increases in computational time (*i.e.*, due to an enormous increase in the number of points in the FID and spectrum, vast spectral widths, *etc.*). Since the full density operator is utilized, it is still possible to see influences of population transfer and/or multiple quantum coherences involving the $\pm 3/2$ spin states and the STs on the CT pattern (*vide infra*). The FS pulses all perform similarly, although none of these generates a powder pattern that compares well with the ideal pattern in

terms of overall signal intensity (*i.e.*, these spectra are all approximately half the total intensity of the ideal pattern and also feature "dips" in intensity on the low frequency sides of the patterns near the orientation of the crystallite tensor orientations with $\beta_Q = 54.74°$, *vide infra*).

Experimental spectra acquired with CPMG-type sequences (Fig. 10, right column) all feature dips on the right side of the patterns (in agreement with simulations) and reduced intensity of the rightmost "horns" (in disagreement with simulations). All three FS pulses perform very similarly in terms of overall pattern shape and signal intensity. HS pulses are effective for acquiring half-integer quadrupolar patterns, but have been used only for purposes of population transfer [32,33,67], and not to excite and refocus the spin polarization associated with the CT (as in the present work). It is possible that for the small portion of the ST powder patterns that the pulse sweeps over, there is some transfer of spin populations that impacts the overall signal (*vide infra*).

#### 3.5.2. Performance of OCTOBER pulses

Numerical simulations of OCTOBER pulses were used in spin-echo pulse sequences (Fig. 11, middle column). These simulations predict increased signal enhancements in comparison to the WURST-echo spectrum. However, these spectra have distortions (dips) on the low-frequency sides of the patterns that are more prominent than the spectra acquired with their unoptimized counterparts. O'Dell et al. showed that pulses optimized for the CT spectra of half-integer quadrupoles excite frequencies corresponding to
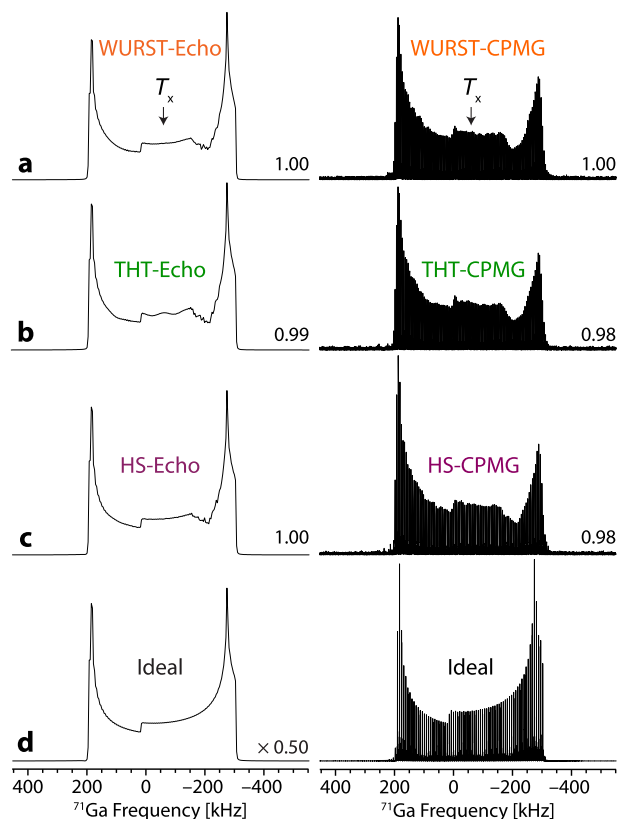
**Fig. 10.** Simulated (left) and experimental (right) $^{71}$Ga NMR spectra of GaPcCl acquired using a pulse sequence (a) with WURST pulses, (b) THT pulses, and (c) HS pulses. (d) Ideal patterns generated using rectangular pulses of infinite power (left Hahn-echo; right CPMG). The transmitter offset frequency is set to *ca.* −60 kHz (*i.e.*, −60 kHz with respect to $\nu_0(^{71}$Ga)) for acquisition of all $^{71}$Ga spectra. Pulses used to acquire these spectra had values of $\tau_p = 40$ μs and $N_p = 600$. Relative simulated and experimental integrated intensities are shown, normalized with respect to the spectra acquired with the WURST-echo and WURST-CPMG sequences, respectively.

the ST patterns, resulting in population transfers and enhancement of the CT [53]; hence, population transfers may also be occurring during these pulses that ultimately cause distortions in the CT powder patterns (*vide infra*).

The OCTOBER pulses were tested experimentally in spin-echo pulse sequences (Fig. 11, right column; a larger array of tests in shown in Fig. S9). The HS-OCTOBER-**REseq** and THT-OCTOBER-**REseq** pulses produce spectra with significantly higher signal intensities than those acquired with the WURST-echo sequence (up to 44% more signal in the case of the THT-OCTOBER-**REseq** spectrum); much of this intensity may arise from the higher maximum and average RF amplitudes that are calculated for the optimized pulse shapes. WURST pulses used for this pattern feature an experimentally optimized RF amplitude. Again, if these WURST pulses were to be used with the same maximum RF as OCTOBER pulses, their performance diminishes greatly in terms of generating patterns of high intensity and uniformity. All of these spectra have the aforementioned "dip" near *ca.* 200 kHz, in agreement with simulations. The OCTOBER amplitude and phase modulations are all described by rapidly fluctuating functions that are discontinuous at some points. Similar types of pulse modulations have been shown for other excitation pulse optimizations for half-integer quadrupolar nuclei, but with narrower patterns [53,54]. These rapid modulations are only produced for half-integer quadrupoles, likely due to the underlying satellite transitions (*N.B.*: the entire $4 \times 4$ density matrix is utilized in the pulse optimization). These considerations may be crucial for the future design, optimization, and application of OCTOBER pulses for acquiring UWNMR spectra.

### 3.5.3. Spin Dynamics

The full density matrix for a $I = 3/2$ ensemble is a $4 \times 4$ square matrix; however, only the CT pattern is detected (*N.B.*, the appearance of this pattern can be influenced by population transfers between the +3/2, +1/2, −1/2, and −3/2 spin states). In order to monitor the spin polarization for this system,

$$\langle \mathbf{I}_z \rangle^{CT} = (\rho_{22} - \rho_{33})/2 \tag{3.2}$$

is tracked for several crystallite tensor orientations in order to monitor the *z*-projection of spin-polarization for only the CT. In this case, $\beta_Q$ represents the angle between the magnetic field, $\mathbf{B}_0$, and the largest component of the EFG tensor, $V_{33}$ (Fig. S5b). The orientation dependence for the angle set for CT patterns of a spin-3/2 nucleus is different than that of spin-1/2 nuclei (Fig. 12).

Fig. 12a shows the *z*-component of spin polarization at various times during the WURST-echo pulse sequence. The excitation pulse is not efficient for generating transverse spin polarization (Fig. 12a, left); however, the refocusing pulse is somewhat efficient for returning the polarization to the *xy*-plane (Fig. 12a, right). During the THT-OCTOBER-**REseq** excitation pulse (Fig. 12b, left), the $\langle \mathbf{I}_z \rangle^{CT}$ components of spin polarization appear to vary more erratically over the course of the pulse than those of the similar WURST pulse in Fig. 12a; this could be due to the discontinuous line shapes of the amplitude and phase modulations of these pulses. However, the generation of transverse spin polarization is improved in comparison to WURST-echo excitation. The subsequent THT-OCTOBER-**REseq** refocusing pulse returns much more of the polarization to the transverse plane than the corresponding WURST refocusing
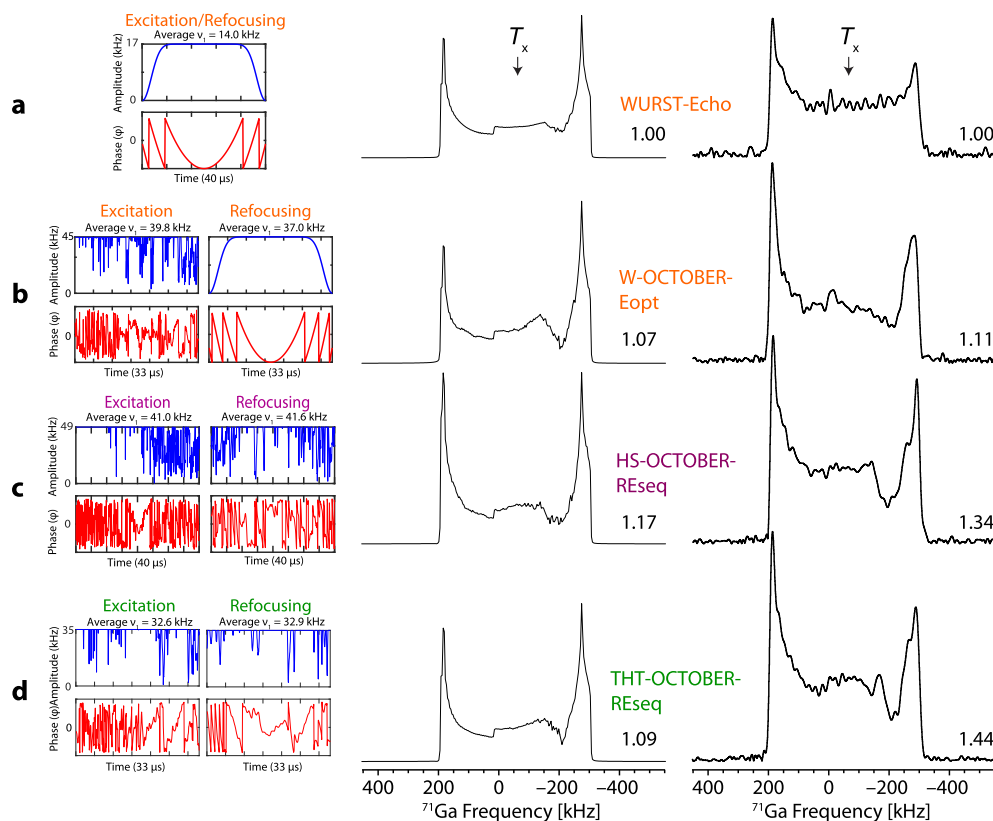


**Fig. 11.** RF amplitude and phase modulation profiles (left column) and simulated (middle column) and experimental (right column) $^{71}$Ga NMR spectra of GaPcCl for the spin-echo pulse sequences utilizing the following pulses: (a) WURST, (b) W-OCTOBER-**Eopt**, (c) HS-OCTOBER-**REseq**, and (d) THT-OCTOBER-**REseq**. Relative simulated and experimental integrated intensities are shown, normalized with respect to the spectrum acquired with the WURST-echo sequence.
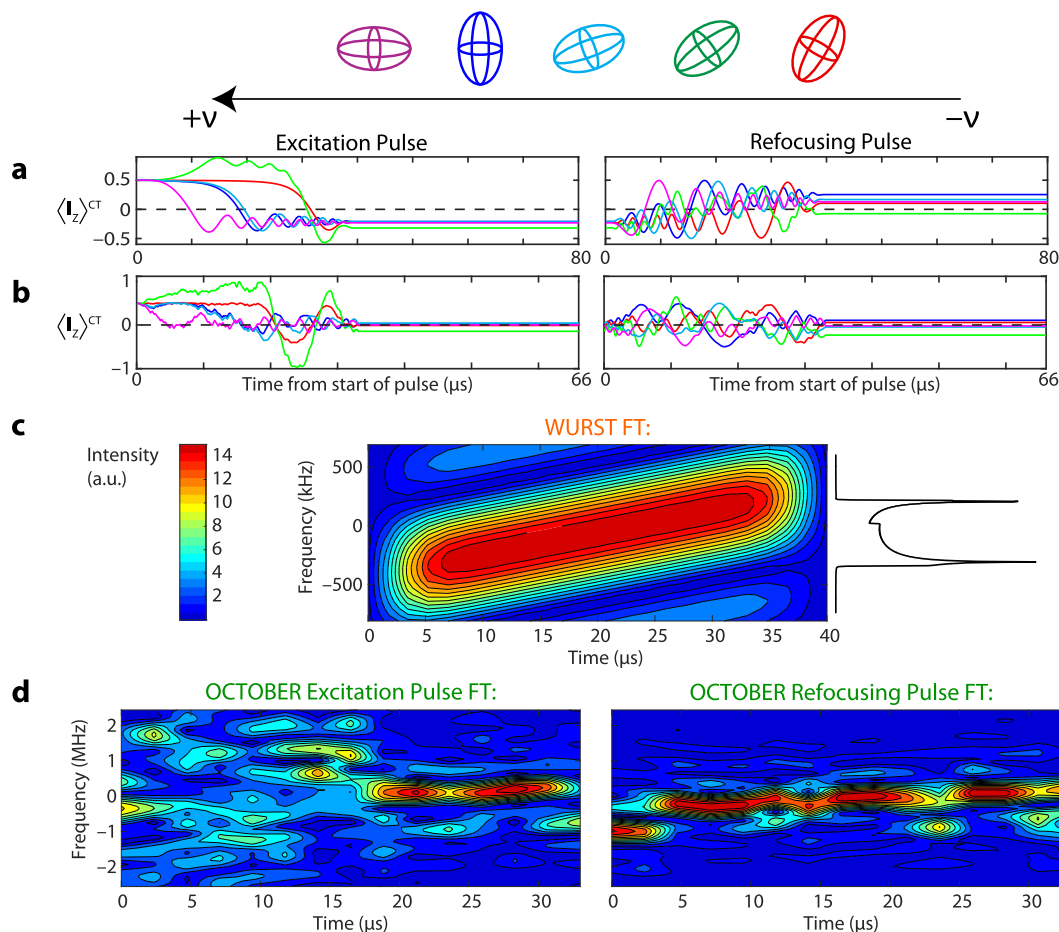
**Fig. 12.** Evolution of the *z*-component of the spin polarization for crystallite tensor orientations ($\beta = 90°$ (purple), $0°$ (navy), $30°$ (cyan), $54.745°$ (green), and $70°$ (red)) (a) during a spin-echo pulse sequence utilizing WURST pulses (sweeping in a low- to high-frequency direction), and (b) during a spin-echo pulse sequence utilizing THT-OCTOBER-**REseq** pulses. Time-resolved Fourier transforms of (c) WURST and (d) THT-OCTOBER-**REseq** pulses. All pulse parameters are described in Fig. 11. (For interpretation of the references to colour in this figure legend, the reader is referred to the web version of this article.)

pulse. The result is an enhancement of signal in comparison to the WURST-echo spectrum (in both simulations and experiment).

The WURST pulse used for this system uniformly sweeps the bandwidth of the CT powder pattern (between *ca.* +200 to −300 kHz, Fig. 12c). The THT-OCTOBER-**REseq** excitation pulse initially excites frequencies far past the CT bandwidth (as broad as *ca.* ±2 MHz (Fig. 12d)). About halfway through the pulse, the excitation profile is much closer to the frequency range of the CT powder pattern. By contrast, the refocusing pulse influences spin polarization only in the frequency range of the CT powder pattern. These results suggest that OCTOBER pulses might influence population transfer for crystallites involved with the STs in order to enhance signal for the CT (*vide infra*). This observation is consistent with previous observations for pulses optimized for half-integer spin systems [53,54].

A final comment should be made on the "dips" *ca.* −200 kHz from the transmitter, which are observed both in simulations and experimentally acquired spectra. This position in the $^{71}$Ga CT spectrum corresponds to the $\beta_Q = 54.745°$ (*i.e.*, magic angle), $\alpha_Q = 0°$ crystallite tensor orientation (Fig. S5b). Only this orientation has values exceeding $\pm 0.5$ for $\langle \mathbf{I}_z \rangle^{CT}$ and always ends up below the *xy*-plane for both simulations of the experiments involving WURST and OCTOBER pulses. This can only arise from population transfers from the $\pm 3/2$ spin states. A detailed analysis of this is ongoing and beyond the current scope of this work; however, a preliminary investigation into these phenomena is presented in Fig. S10.

## 4. Conclusions

FS pulses, including WURST, THT, and HS pulses, have been implemented in spin-echo and CPMG-type pulse sequences for the acquisition of UWNMR patterns of spin-1/2, integer-spin, and half-integer quadrupolar nuclei. This is the first report of the successful implementation of THT and HS pulses for broadband excitation and refocusing for the acquisition of UWNMR spectra. A detailed analysis demonstrates that (i) THT and WURST pulses outperform HS pulses for the acquisition of broad spin-1/2 patterns, as evident in the simulations and experiments on $^{119}$Sn and $^{195}$Pt systems; and (ii) THT and HS pulses are as efficient as WURST pulses for the acquisition of broad quadrupolar patterns, as demonstrated by simulations and experiments on $^2$H and $^{71}$Ga systems.

The three types of FS pulses have been utilized as starting functions for the generation of new pulses using OCT that are capable of efficient broadband excitation and refocusing. These so-called OCTOBER pulses are effective for the acquisition of UWNMR spectra using spin-echo sequences in both simulation and experiment (their implementation in CPMG schemes is beyond the scope of the current work, but certainly of future interest). Additionally, OCTOBER pulses were used in a preliminary investigation of Bloch-decay experiments for the acquisition of a broad pattern of a spin-1/2 nucleus ($^{119}$Sn). This may be greatly beneficial for samples possessing nuclei with short $T_2$ values and broad powder patterns, since their spectra cannot

be acquired using conventional spin-echo or CPMG sequences. Furthermore, the use of a single pulse that simultaneously prefocuses magnetization may allay concerns regarding acoustic ringing prior to turning on the receiver [44].

Three methods of OCT pulse optimization (**Eopt**, **ERopt**, and **REseq**) have been shown to be effective in different cases, though there are no general trends for selecting one method over another, due to the limited number of systems investigated to date. Furthermore, the choices of WURST, THT, or HS pulses as starting functions impacts the performance of the generated OCTOBER pulses for different nuclei. For instance, the use of THT-OCTOBER pulses was the most successful for the acquisition of $^{119}$Sn, $^{195}$Pt, and $^{71}$Ga spectra; this may be because these spectra arise from SQ transitions (with minor exceptions for $^{71}$Ga and its underlying ST patterns, *vide supra*). On the other hand, HS-OCTOBER pulses worked well for acquiring $^{2}$H and $^{71}$Ga spectra, perhaps due to the presence of overlapping SQ transitions (*i.e.*, $0 \longleftrightarrow \pm1$ STs for $^{2}$H and CT and STs for $^{71}$Ga). Further work must be done to evaluate the reasons for these differences in performance.

Careful consideration must be given to the maximum allowable RF amplitude utilized for the general FS pulses (*i.e.*, WURST, THT, and HS) and OCTOBER pulses generated from these pulses. FS pulses are tested and implemented with experimentally optimized maximum RF amplitudes. Conversely, OCTOBER pulses are almost always successfully implemented with maximum RF amplitudes that are greater than those used in experiments featuring the FS pulses. Importantly, if the higher RF amplitudes predicted by OCT are used in experiments featuring FS pulses, the resulting powder patterns are always lower in signal intensity and non-uniformly excited. Fortunately, the average RF amplitudes for most OCTOBER pulses are significantly lower than the maximum amplitude, making their power requirements feasible for most spectrometers and probes.

Finally, examination of the time evolution of the spin polarization during the FS and OCTOBER pulses provides a means of analyzing the mechanisms and spin dynamics underlying these pulse sequences and assists in explaining cases of poor or exceptional performance. This is aided by using time-resolved Fourier analysis of the pulses, which serves to reveal the time-dependent effective bandwidths of the excitation and refocusing pulses. At the current time, only the spin-1/2 systems have been thoroughly investigated. The $^{71}$Ga ($I = 3/2$) and $^{2}$H ($I = 1$) systems are complicated by overlapping patterns and MQ coherences; thorough investigations of these systems are beyond the scope of this work, but currently under investigation by our group. In select cases for OCTOBER pulses, this is revealed as combinations of three general features: (i) linear frequency sweeps, (ii) sporadic linear frequency-sweep behaviour with rapidly changing sweep directions, and (iii) stationary (*i.e.*, no frequency sweep) homogeneous excitation. This type of analysis may potentially suggest pathways to new pulse parameterizations or even generalized pulses that are superior to conventional FS pulses.

## Acknowledgements

## Appendix A. Supplementary material

Supplementary data to this article can be found online at https://doi.org/10.1016/j.jmr.2019.106612.

## References

[1] R.W. Schurko, Acc. Chem. Res. 46 (2013) 1985–1995.
[2] R.W. Schurko, Acquisition of wideline solid-state NMR spectra of quadrupolar nuclei, in: Encyclopedia of Magnetic Resonance, John Wiley & Sons Ltd, Chichester, UK, 2011, pp. 77–93.
[3] D. Massiot, I. Farnan, N. Gautier, D. Trumeau, A. Trokiner, J. Pierre, Solid State Nucl. Magn. Reson. 4 (1995) 241–248.
[4] A. Medek, V. Frydman, L. Frydman, J. Phys. Chem. B 5647 (1997) 8959–8966.
[5] E.L. Hahn, Phys. Rev. 80 (1950) 580–594.
[6] S.E. Shore, J. Ansermet, C.P. Slichter, J.H. Sinfelt, Phys. Rev. Lett. 58 (1987) 953–956.
[7] H.Y. Carr, E.M. Purcell, Phys. Rev. 94 (1954) 630–638.
[8] S. Meiboom, D. Gill, Rev. Sci. Instrum. 29 (1958) 688–691.
[9] F.H. Larsen, H.J. Jakobsen, P.D. Ellis, N.C. Nielsen, J. Phys. Chem. A 101 (1997) 8597–8606.
[10] I. Hung, Z. Gan, J. Magn. Reson. 204 (2010) 256–265.
[11] O. Pecher, D.M. Halat, J. Lee, Z. Liu, K.J. Griffith, M. Braun, C.P. Grey, J. Magn. Reson. 275 (2017) 127–136.
[12] Z. Gan, P. Gor'Kov, T.A. Cross, A. Samoson, D. Massiot, J. Am. Chem. Soc. 124 (2002) 5634–5635.
[13] T. Kobayashi, Y. Nishiyama, M. Pruski, Heteronuclear correlation solid-state NMR spectroscopy with indirect detection under fast magic-angle spinning, Modern Methods in Solid State NMR, Royal Society of Chemistry, 2018.
[14] A.J. Rossini, M.P. Hanrahan, M. Thuo, Phys. Chem. Chem. Phys. 18 (2016) 25284–25295.
[15] V. Vitzthum, M.A. Caporini, S. Ulzega, G. Bodenhausen, J. Magn. Reson. 212 (2011) 234–239.
[16] A.B. Barnes, M.L. Mak-jurkauskas, Y. Matsuki, V.S. Bajaj, P.C.A. Wel, Van Der, R. Derocher, J. Bryant, J.R. Sirigiri, R.J. Temkin, J. Lugtenburg, et al., J. Magn. Reson. 198 (2009) 261–270.
[17] M. Rosay, L. Tometich, S. Pawsey, R. Bader, R. Schauwecker, M. Blank, P.M. Borchard, S.R. Cauffman, K.L. Felch, R.T. Weber, et al., Phys. Chem. Chem. Phys. 12 (2010) 5850–5860.
[18] T. Kobayashi, F.A. Perras, A. Murphy, Y. Yao, J. Catalano, S.A. Centeno, C. Dybowski, N. Zumbulyadis, M. Pruski, Dalt. Trans. 46 (2017) 3535–3540.
[19] D.A. Hirsh, A.J. Rossini, L. Emsley, R.W. Schurko, Phys. Chem. Chem. Phys. 18 (2016) 25893–25904.
[20] A. Tannús, M. Garwood, NMR Biomed. 10 (1997) 423–434.
[21] Ē. Kupce, R. Freeman, J. Magn. Reson. Ser. A 117 (1995) 246–256.
[22] R. Bhattacharyya, L. Frydman, J. Chem. Phys. (2007) 127.
[23] L.A. O'Dell, R.W. Schurko, Chem. Phys. Lett. 464 (2008) 97–102.
[24] K.J. Harris, A. Lupulescu, B.E.G. Lucier, L. Frydman, R.W. Schurko, J. Magn. Reson. 224 (2012) 38–47.
[25] L.A. O'Dell, Solid State Nucl. Magn. Reson. 55–56 (2013) 28–41.
[26] L.A. O'Dell, A.J. Rossini, R.W. Schurko, Chem. Phys. Lett. 468 (2009) 330–335.
[27] M. Garwood, L. DelaBarre, J. Magn. Reson. 153 (2001) 155–177.
[28] Y.A. Tesiram, M.R. Bendall, J. Magn. Reson. 156 (2002) 26–40.
[29] T.L. Hwang, P.C.M. Van Zijl, M. Garwood, J. Magn. Reson. 133 (1998) 200–203.
[30] M.S. Silver, R.I. Joseph, D.I. Hoult, J. Magn. Reson. 59 (1984) 347–351.
[31] R. Siegel, T.T. Nakashima, R.E. Wasylishen, Chem. Phys. Lett. 403 (2005) 353–358.
[32] R. Siegel, T.T. Nakashima, R.E. Wasylishen, Chem. Phys. Lett. 421 (2006) 529–533.
[33] M.R. Hansen, M. Brorson, H. Bildsøe, J. Skibsted, H.J. Jakobsen, J. Magn. Reson. 190 (2008) 316–326.
[34] F.A. Perras, J. Viger-Gravel, K.M.N. Burgess, D.L. Bryce, Solid State Nucl. Magn. Reson. 51–52 (2013) 1–15.
[35] N. Khaneja, T. Reiss, C. Kehlet, T. Schulte-Herbrüggen, S.J. Glaser, J. Magn. Reson. 172 (2005) 296–305.
[36] P.De. Fouquieres, S.G. Schirmer, S.J. Glaser, I. Kuprov, J. Magn. Reson. 212 (2011) 412–417.
[37] D.L. Goodwin, I. Kuprov, J. Chem. Phys. (2016) 204107.
[38] S.J. Glaser, U. Boscain, T. Calarco, C.P. Koch, W. Köckenberger, R. Kosloff, I. Kuprov, B. Luy, S. Schirmer, T. Schulte-Herbrüggen, et al., Eur. Phys. J. D 69 (2015) 279.
[39] T.E. Skinner, T.O. Reiss, B. Luy, N. Khaneja, S.J. Glaser, J. Magn. Reson. 163 (2003) 8–15.
[40] T.E. Skinner, T.O. Reiss, B. Luy, N. Khaneja, S.J. Glaser, J. Magn. Reson. 167 (2004) 68–74.
[41] K. Kobzar, T.E. Skinner, N. Khaneja, S.J. Glaser, B. Luy, J. Magn. Reson. 170 (2004) 236–243.
[42] K. Kobzar, T.E. Skinner, N. Khaneja, S.J. Glaser, B. Luy, J. Magn. Reson. 194 (2008) 58–66.
[43] T.E. Skinner, K. Kobzar, B. Luy, M.R. Bendall, W. Bermel, N. Khaneja, S.J. Glaser, J. Magn. Reson. 179 (2006) 241–249.
[44] N.I. Gershenzon, T.E. Skinner, B. Brutscher, N. Khaneja, M. Nimbalkar, B. Luy, S. J. Glaser, J. Magn. Reson. 192 (2008) 235–243.

[45] T.E. Skinner, N.I. Gershenzon, M. Nimbalkar, W. Bermel, B. Luy, S.J. Glaser, J. Magn. Reson. 216 (2012) 78–87.
[46] K. Kobzar, S. Ehni, T.E. Skinner, S.J. Glaser, B. Luy, J. Magn. Reson. 225 (2012) 142–160.
[47] M. Braun, S.J. Glaser, New J. Phys. (2014) 16.
[48] T.T. Nguyen, S.J. Glaser, J. Magn. Reson. 282 (2017) 142–153.
[49] W. Kallies, S.J. Glaser, J. Magn. Reson. 286 (2018) 115–137.
[50] T.W. Borneman, M.D. Hürlimann, D.G. Cory, J. Magn. Reson. 207 (2010) 220–233.
[51] Z. Tošner, T. Vosegaard, C. Kehlet, N. Khaneja, S.J. Glaser, N.C. Nielsen, J. Magn. Reson. 197 (2009) 120–134.
[52] H.J. Hogben, M. Krzystyniak, G.T.P. Charnock, P.J. Hore, I. Kuprov, J. Magn. Reson. 208 (2011) 179–194.
[53] L.A. O'Dell, K.J. Harris, R.W. Schurko, J. Magn. Reson. 203 (2010) 156–166.
[54] L.A. O'Dell, C.I. Ratcliffe, J. Phys. Chem. A 115 (2011) 747–752.
[55] A.W. MacGregor, L.A. O'Dell, R.W. Schurko, J. Magn. Reson. 208 (2011) 103–113.
[56] M. Bak, J.T. Rasmussen, N.C. Nielsen, J. Magn. Reson. 213 (2011) 366–400.
[57] C. Müller, W. Schajor, H. Zimmermann, U. Haeberlen, J. Magn. Reson. 56 (1984) 235–246.
[58] P. Pyykkö, Mol. Phys. 99 (2009) 1617–1629.
[59] R.K. Harris, E.D. Becker, M. Cabral de Menezes, R. Goodfellow, P. Granger, Solid State Nucl. Magn. Reson. 22 (2002) 458–483.
[60] K. Takegoshi, M. Ito, T. Terao, Chem. Phys. Lett. 2614 (1996) 159–165.
[61] J.A. Tang, L.A. O'Dell, P.M. Aguiar, B.E.G. Lucier, D. Sakellariou, R.W. Schurko, Chem. Phys. Lett. 466 (2008) 227–234.
[62] C. Cossement, J. Darville, J. Gilles, J.B. Nagy, C. Fernandez, J.P. Amoureux, Magn. Reson. Chem. 30 (1992) 263–270.
[63] J.R. Johansson, P.D. Nation, F. Nori, Comput. Phys. Commun. 183 (2012) 1760–1772.
[64] L.A. O'Dell, R.W. Schurko, J. Am. Chem. Soc. 131 (2009) 6658–6659.
[65] S.L. Veinberg, Z.W. Friedl, A.W. Lindquist, B. Kispal, K.J. Harris, L.A. O'Dell, R.W. Schurko, ChemPhysChem 17 (2016) 4011–4027.
[66] S.L. Veinberg, A.W. Lindquist, M.J. Jaroszewicz, R.W. Schurko, Solid State Nucl. Magn. Reson. (2016) 1–14.
[67] L.A. O'Dell, K. Klimm, J.C.C. Freitas, S.C. Kohn, M.E. Smith, Appl. Magn. Reson. 35 (2009) 247–259.